

Ultrahigh-field 9.4T MRI for Evaluating Neonatal Piglet Brain

By

Szumo Wang

B.S., National Chiayi University, Taiwan (ROC), 2016

THESIS

Submitted as partial fulfillment of the requirements
for the degree of Master of Science in Bioengineering
in the Graduate College of the
University of Illinois at Chicago, 2021

Chicago, Illinois

Defense Committee:

Weiguo Li, Ph.D., Chair and Advisor

Richard L. Magin, Ph.D., Department of Bioengineering, UIC

Kelly A. Tappenden., Ph.D., Department of Kinesiology and Nutrition, UIC

ACKNOWLEDGEMENTS

I am grateful to many individuals who have supported and helped me in the process of completing the thesis. First and foremost, I would like to express my gratitude to my family members for their unconditional support and encouragement, especially to my father who believed in me and supported me in my studies. I would like to express my appreciation to my advisor, Dr. Weiguo Li for providing this interesting project and for all his support, assistance, and guidance throughout the work. I would also like to thank Dr. Kelly A. Tappenden and Dr. Yimin Chen for providing the resources so that this project could be fulfilled.

I would like to extend my appreciation to Dr. Richard L. Magin for his input and comments, to my colleague Jin Gao for her assistance on the acquisition of MR images, and to Riken Patel and Kevin Hu for their support on image processing.

Finally, I would like to give special thanks to my close friends, especially to Songyun Liu and Jade He, for their suggestions and encouragement. Without all these individuals noted above this project would not have been accomplished.

CONTRIBUTION OF AUTHORS

Chapter 1 is the introduction that includes the background, the motivation, and the thesis objectives. Chapter 2 provides the basic concept of the MRI. Chapter 3 reviews the knowledge of brain we have to date including the general brain knowledge, the early human brain development, the advantages of the pig brain as an alternative of human brain, and the knowledge of early piglet brain development. Chapter 4 and Chapter 5 are the unpublished work mainly driven by me, with Dr. Kelly A. Tappenden and Dr. Yimin Chen provided the subjects Dr. Weiguo Li helped set up the scanning protocol, Jin Gao assisted me acquiring the images, and Riken Patel as well as Kevin Hu provided peer reviews with the segmentation. Chapter 6 represents my overall conclusions and the direction of future works.

TABLE OF CONTENTS

1. INTRODUCTION	1
1.1. BACKGROUND.....	1
1.2. MOTIVATION	2
1.3. THESIS OBJECTIVES	2
2. MAGNETIC RESONANCE IMAGING.....	3
2.1. THE PRINCIPLES OF MRI.....	3
2.1.1. <i>Nuclear Magnetic Resonance Theory</i>	3
2.1.2. <i>The Physics of Spin</i>	4
2.1.3. <i>Radio-frequency Pulse Excitation</i>	5
2.1.4. <i>Spin-lattice and Spin-spin Relaxation</i>	6
2.1.5. <i>Repetition Time (TR) and Time to Echo (TE)</i>	8
2.1.6. <i>Free Induction Decay</i>	9
2.2. THE ELEMENTS OF MR IMAGING	10
2.2.1. <i>T₁, T₂, and Proton-density Weighting Image Contrast</i>	10
2.2.2. <i>Image Acquisition</i>	10
2.2.3. <i>Fast Spin Echo Sequence</i>	14
2.2.4. <i>Three-dimensional Imaging</i>	15
3. BRAIN DEVELOPMENT	16
3.1. THE BRAIN IN GENERAL	16
3.2. HUMAN BRAIN DEVELOPMENT AND INTELLIGENCE	19
3.3. ANIMAL MODELS FOR BRAIN RESEARCH	20

3.4.	PIGLET BRAIN	20
4.	EVALUATION OF PIGLET BRAIN STRUCTURES WITH <i>EX VIVO</i> IMAGES	22
4.1.	INTRODUCTION	22
4.2.	MATERIAL AND METHODS	24
4.2.1.	<i>Specimen preparation</i>	24
4.2.2.	<i>MRI acquisition</i>	24
4.2.3.	<i>Delineation and segmentation</i>	24
4.2.4.	<i>Analysis of the volumes of the structures</i>	25
4.3.	RESULTS	25
4.3.1.	<i>Piglet brain segmentation</i>	25
4.3.2.	<i>Volumetric analysis</i>	29
4.4.	DISCUSSION	32
4.5.	SUMMARY	36
5.	<i>IN VIVO</i> AND <i>EX VIVO</i> PIGLET BRAIN COMPARISON	37
5.1.	INTRODUCTION	37
5.2.	MATERIALS AND METHODS	38
5.2.1.	<i>Specimen preparation</i>	38
5.2.2.	<i>MRI acquisition</i>	38
5.2.3.	<i>Delineation and segmentation</i>	39
5.2.4.	<i>Analysis of structure volumes and statistics</i>	39
5.3.	RESULTS	40
5.3.1.	<i>Piglet brain segmentation</i>	40
5.3.2.	<i>Analysis of the volumes of the structures</i>	42

5.4.	DISCUSSION	55
5.5.	SUMMARY	57
6.	CONCLUSION	58
6.1.	SUMMARY	58
6.2.	FUTURE WORK	59
7.	REFERENCES	60
8.	VITA	72

LIST OF TABLES

<i>Table I. Intervals for image weighting.....</i>	<i>10</i>
<i>Table II. Statistics of piglet brain structures</i>	<i>31</i>
<i>Table III. Findings between Conrad's work and our data.</i>	<i>32</i>
<i>Table IV. Image resolution for fourteen low-resolution images.....</i>	<i>42</i>

LIST OF FIGURES

<i>Figure 1. Spin physics: (A) In ordinary situations, each spin points in a random direction. (B) The spin aligns parallel or antiparallelly to an external B_0 field.</i>	<i>5</i>
<i>Figure 2. The spins generate a net magnetization that aligns with the external magnetic field while precessing around the z-axis. When a 90° RF pulse is applied, the net magnetization is flipped to the x-y plane and it precesses in the x-y plane.</i>	<i>6</i>
<i>Figure 3. T_1 and T_2 relaxation: After the RF pulse is turned off, longitudinal magnetization, or T_1 relaxation, starts to recover. T_1 relaxation time is the time needed for T_1 relaxation to reach 63% of maximum magnetization. At the same time, transverse magnetization, or T_2 relaxation, starts to decay. The T_2 relaxation time is the time needed for T_2 relaxation to decay to 37% of its initial magnetization.</i>	<i>7</i>
<i>Figure 4. Free induction decay: The signal received by the receiver coil gradually decays as the spins recover to their original state, after the RF pulse is turned off.</i>	<i>9</i>
<i>Figure 5. Slice-selection: The slice-selection gradient is used to select a specific slice of interest. The gradient creates a slightly different field along the subject. To excite a specific slice, a specific RF pulse is transmitted, which matches the spin-precessing frequency in the tissue in the slice.</i>	<i>11</i>
<i>Figure 6. The phase-encoding gradient: By applying a phase gradient along the y axis (as in this example), the spins of the lines experience different magnetic fields and precess differently according to the field.</i>	<i>12</i>
<i>Figure 7. The frequency-encoding gradient: After applying the phase-encoding gradient along the y-axis, the frequency-encoding gradient is applied along the x-axis. As a result, the spin in each grid precesses differently.</i>	<i>13</i>

<i>Figure 8. High-resolution images of 15 segmented structures of the piglet brain. (A) The raw image of coronal view. (B) The raw image of axial view. (C) The raw image of sagittal view. (D) The coronal view after segmentation. (E) The axial view after segmentation. (F) The sagittal view after segmentation. (G) Segmentation labels.</i>	<i>27</i>
<i>Figure 9. The three-dimensional model of the piglet brain reconstructed from three-dimensional T₂-weighted images: (A) The left-right view. (B) The superior-inferior view.</i>	<i>28</i>
<i>Figure 10. Illustrations of 15 segmented structures of the piglet brain.</i>	<i>29</i>
<i>Figure 11. Mean volumes of 15 structures of the piglet brain.....</i>	<i>30</i>
<i>Figure 12. The percentages of the structures of the piglet brain.....</i>	<i>32</i>
<i>Figure 13. Reconstructions of high- and low-resolution T₂-weighted piglet brain images with six structures: (A) The coronal view of in vivo piglet brain image. (B) Reconstructed model from in vivo piglet brain images. (C) The coronal view of ex vivo piglet brain. (D) Reconstructed model from ex vivo piglet brain images. The hippocampal region is labeled in red in this image; the cerebral cortex along with the other parts of the brain are labeled in green in this image; cerebellum which is in the lower part of the image is labeled in yellow; the thalamus is in the middle part of the brain near the hippocampus with the light blue label; the midbrain is the structure that locates between the thalamus and the cerebellum is labeled with grey-blue, and the olfactory bulb that is in the upper part of the image is labeled with pink.</i>	<i>41</i>
<i>Figure 14. Volumes of structures from high- and low-resolution images at different image resolutions: (A) The cerebellum volume. (B) The midbrain volume. (C) The thalamus volume. (D) The olfactory bulb volume. (E) The hippocampus volume. (F) The whole-brain volume.</i>	<i>44</i>
<i>Figure 15. Plots of volumes of structures from high-resolution and low-resolution images with different image resolutions: (A) The cerebellum volume. (B) The midbrain volume. (C) The</i>	

thalamus volume. (D) The olfactory bulb volume. (E) The hippocampus volume. (F) The whole-brain volume. Orange line is the ideal volume for the low-resolution images; Gray dotted lines are the acceptable margins of error for each structure; Blue dots represent R1; Yellow dots represent R2. 46

Figure 16. Plots of the volumes of brain structures at low-resolution and high-resolution with Pearson correlation analysis: (A) The cerebellum volume. (B) The midbrain volume. (C) The plot of thalamus volume. (D) The olfactory bulb volume. (E) The hippocampus volume. (F) The whole-brain volume. 48

Figure 17. Bland-Altman plots of differences in volume from high-resolution and low-resolution images: (A) Cerebellum volume. (B) Midbrain volume. (C) Thalamus volume. (D) Olfactory bulb volume. (E) Hippocampus volume. (F) Whole-brain volume. 51

Figure 18. Result of paired t-tests to compare the volumes from high- and low-resolution images for six brain structures, using resolution R1. (A) The cerebellum volume. (B) The midbrain volume. (C) The thalamus volume. (D) The olfactory bulb volume. (E) The hippocampus volume. (F) The total volume of the brain. 53

Figure 19. Result of paired t-tests to compare the volumes from high- and low-resolution images for six brain structures, using resolution R2. (A) The cerebellum volume. (B) The midbrain volume. (C) The thalamus volume. (D) The olfactory bulb volume. (E) The hippocampus volume. (F) The total volume of the brain. 55

LIST OF ABBREVIATIONS

3D	Three-dimensional
ADH	Antidiuretic hormone
ATCH	Adrenocorticotrophin
B_0	External magnetic field
B_1	Radio-frequency field
CI	Confidence intervals
CSE	Conventional spin echo
CV	Coefficient of variation
ETL	Echo train length
ESP	Echo space
FID	Free induction decay
FSE	Fast spin echo
FSH	Follicle-stimulating hormone
GH	Growth hormone
G_{freq}	Frequency-encoding gradient
G_{phase}	Phase-encoding gradient
G_{slice}	Slice-selection gradient
IQ	Intelligence quotient
LH	Luteinizing hormone
LOA	Limits of agreement
M_0	Net magnetization
MDM	Magnetic dipole moment

MRI	Magnetic resonance imaging
MSH	Melanocyte-stimulating hormone
NEX	Number of Excitation
NMR	Nuclear magnetic resonance
OXT	Oxytocin
PET	Positron emission tomography
PRL	Prolactin
r	Pearson correlation coefficient
R^2	Coefficient of determination
RF	Radio-frequency
ROI	Region of Interest
T	Tesla
T_1	Longitudinal relaxation
T_2	Transverse relaxation
T_2^*	T_2 star relaxation
TE	Time to echo
TR	Repetition time
TSH	Thyroid-stimulating hormone

SUMMARY

Understanding normal brain development can provide references for the assessment of brain injury associated with various diseases. As crucial prerequisites to replicate human diseases, suitable animal models are exploited to develop preclinical protocols in biomedical research for diagnosis and therapies. For brain development studies, pig models have increasingly been used because of the similarities in anatomical and physiological characteristics shared by brains of pig and that of humans.

Magnetic resonance imaging (MRI) is a broadly used noninvasive method in the diagnosis of neurological diseases, the monitoring of disease progression, and the assessment of therapeutic efficacy in preclinical research and clinical settings. Although MRI has been used to evaluate the pig brain, there is a lack of study to illuminate the neonatal piglet brain anatomy with high-resolution MRI performed with an ultra-high magnetic field. The first aim of this thesis is to evaluate the anatomical structures of piglet brain and to contribute to the database with 12-day-old piglet brains. Nineteen neonatal female pig brains were scanned *ex vivo* with a 9.4T MR scanner, using a three-dimensional fast spin-echo T₂-weighted sequence to acquire MR images at a resolution of $0.2344 \times 0.2539 \times 0.2539$ mm. Fifteen brain structures were segmented by manual delineation and a 3D piglet brain model was reconstructed. We found that the cerebral cortex, the cerebellum, and the brain stem contributed to 87.1% of the whole brain, while the hippocampus contributed to 2.13% on average. Our second aim is to compare *in vivo* and *ex vivo* MR images for volume measurements of various structures of the piglet brains. Two different image resolutions were applied for *in vivo* MRI. After *in vivo* MRI, piglet head samples were dissected, rapid frozen and stored in -80° freezer for 2 months, and slowly dissolved before acquiring high resolution *ex vivo* MR images. We found brain structures at the back such as the cerebellum and midbrain

showed no difference in volumes between *in vivo* and *ex vivo* images, regardless of using two different resolutions of the *in vivo* images. The measured volumes of structures in the middle such as the hippocampus and thalamus from the high-resolution *ex vivo* images showed no difference to those from *in vivo* images under one resolution (R1), whereas significant volume differences were found when utilizing the *in vivo* image resolution (R2). Structures that have measured volume differences between *in vivo* and *ex vivo* were the olfactory bulb and whole brain, regardless the resolutions of *in vivo* images.

In this study, we measured the volumes of brain structures of 12-day-old piglets and generated a database of piglet brains at ages of 12 days. Our results can provide references for *in vivo* assessment of brain growth in metabolism, nutrition research for pediatric brain development and studies using more advanced image analyzing techniques such as voxel-based morphometry. In addition, our results from *in vivo* and *ex vivo* MR image comparisons can provide guidance for proper handling of brain samples for other studies. Further studies to build a standard neonatal piglet brain atlas and the piglet brain database according to stages of brain development will benefit brain development and neurological studies using piglet as a translational animal model.

1. INTRODUCTION

1.1. BACKGROUND

The human brain is the most complex human organ, and it is the core of all the physical and mental needs of a person [1]. Although we have been studying the brain for decades [1], there is still a great deal to discover [2]. The gaps in our knowledge of the brain makes it difficult to diagnose, analyze, and treat brain disease [1]. Understanding the early development of the brain not only may help us understand long-term neurodevelopment [3], but it also may help prevent potential risks to infants [4]. However, there are ethical and practical issues involved with researching the human brain directly, especially when we want to collect data from infants or fetuses [5]. Therefore, animal models become an alternative way to carry out brain-related experiments. Meanwhile, the pig is an excellent animal model for medical research of the brain [6], and the use of pigs has been increasing in the neuroscience field [7]. Even though the morphology of the pig brain is closer to that of humans than the brains of mice [8], most current knowledge of brain development has been established by analyzing the mouse brain [9]. At the same time, the knowledge of piglet brain development is insufficient [6][7]. To study the brain, a brain atlas is needed to set standards for brain morphology that gives researchers an anatomical view of regional brain structures [3]. To build this brain atlas, a tool is needed, and neuroimaging is a powerful tool that enables us to study the anatomical morphology of the brain [10]. Among all the imaging techniques, magnetic resonance imaging (MRI) is an optimal tool to study the brain for its high contrast sensitivity, high spatial resolution, and ionizing radiation-free performance [11].

1.2. MOTIVATION

For the most part, brains from animal models have been used for neural-related studies instead of conducting experiments directly on the human brain. For decades, it has been known that the piglet brain is an excellent animal model for brain-related research. This is especially true for brain development, since the brain development pattern of the piglet is similar to that of humans. Even though this is not a new concept, the pig brain atlas is not as extensively established as the rodent brain atlas. This is an important gap to fill, as the brain atlas is an essential tool in neuroscience because it provides knowledge of the brain's structural anatomy to researchers. Nevertheless, data on piglet brains at the neonatal age is rare. The overall goal of this thesis is to investigate the anatomies of the brains of domestic neonatal piglets to contribute to the database for eventually building a standard neonatal piglet brain atlas.

1.3. THESIS OBJECTIVES

Specific aim 1 To evaluate the volumes of structures of piglet brain based on high-resolution images.

Specific aim 2 To compare the volumetric differences between high-resolution *ex vivo* images and low-resolution *in vivo* images.

2. MAGNETIC RESONANCE IMAGING

Magnetic resonance imaging (MRI) is derived from the principles of nuclear magnetic resonance (NMR), which has been developed for decades [12]. Not until 1971 was this technique introduced to diagnose cancer [12]. In 1973, the first magnetic resonance image (MRI) was performed by Paul Lauterbur [13]. Since then, MRI techniques have surged in the biomedical field [12]. MRI is well known for its non-invasive, ionizing radiation-free, ability to differentiate tissue, and applicational flexibility [14][15][16]. This has made it a dominant clinical imaging modality [14].

2.1. THE PRINCIPLES OF MRI

2.1.1. Nuclear Magnetic Resonance Theory

As noted above, the MRI is derived from nuclear magnetic resonance (NMR), which has been used for chemical analysis for over 50 years [17]. To understand the concept of the MRI, it a review of NMR theory is useful. NMR was introduced by Felix Bloch. He stated that electromagnetic waves can be generated from any spinning charged isotope because spinning makes an isotope behave like a magnet [13][14][17][18]. For a charged isotope to spin, its nucleus must have an unpaired, or odd, number of protons [17][19]. When the protons in a nucleus are even in number, the magnetic field created by one proton is canceled by the other proton. Then the magnetic field is zero, and there is no electromagnetic wave [17][19].

To perform MRI, we need charged isotopes and multiple elements can be used for MRI. For example, ^1H , ^{13}C , ^{19}F , ^{23}Na , and ^{31}P have odd numbers of protons in their nuclei [17][18]. In clinical MRI, the most widely used nuclei are the proton (^1H) from water, which is abundant in the body and the proton (^1H) from fat is used as well [14][17][18].

2.1.2. The Physics of Spin

Spin is the magnetic moment or so-called magnetic dipole moment (MDM) generated by a spinning charged isotope [14][17]. The magnetic moment can be considered as a vector $\vec{\mu}$ with its direction pointing to the tangent of the spin. This is also known as the angular momentum of the spinning particle, as shown in Eq. (2-1):

$$\vec{\mu} = q/2m \times J \quad (2-1)$$

where q is the charge on the particle, m is the mass of the particle, and J is the angular momentum of the particle [14].

Under ordinary conditions, when there is no influence from a strong external magnetic field, the magnetic moment of each particle spinning around its axes is in a random direction [17]. Thus, the magnetic moments created from spinning particle cancel each other out, so the net magnetization is zero, as shown in Fig. 1 (A) [18]. However, when a strong external magnetic field (B_0) is present, the spinning particles will align either in parallel or antiparallel to it. When enough particles are spinning in parallel (which is their equilibrium state or so-called lowest energy level), a net magnetization (M_0) is created from the sum of the magnetic moments, as shown in Fig. 1 (B) [14][17][18]. When the spinning is parallel or antiparallel with the axes of the external magnetic field (B_0), the spin also precesses, circularly aligning the B_0 field with a certain angle [20]. The angular frequency (ω) precessing around the axes of the B_0 field is defined by the Larmor frequency as shown in Eq. (2-2) [19].

$$\omega = \gamma B_0 \quad (2-2)$$

where the γ is the gyromagnetic ratio and the proton (^1H), which is the dominantly used isotope in MRI, has the value of 42.58 MHz/Tesla [17][18]. Different isotopes have their own gyromagnetic ratios [12].

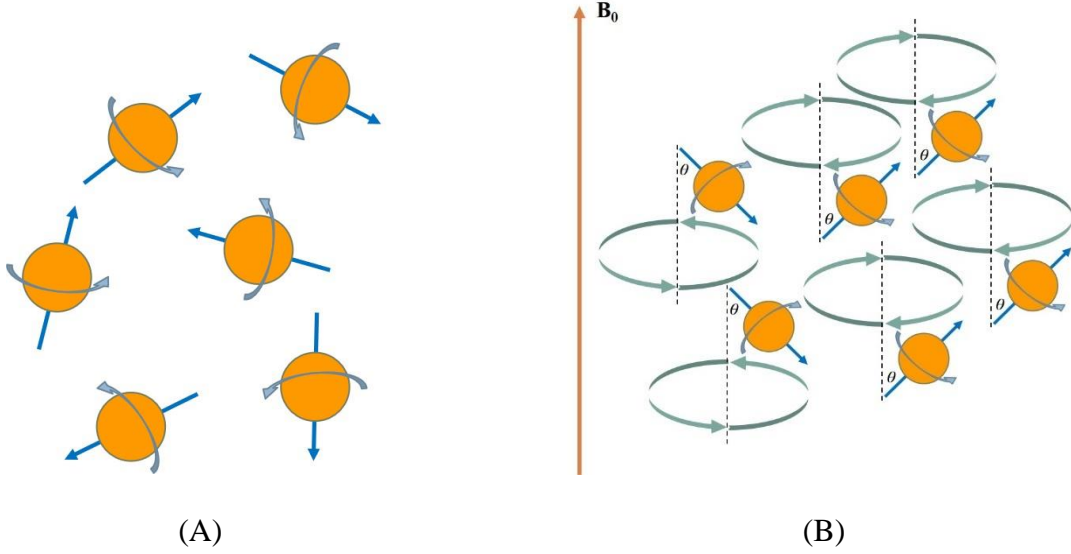


Figure 1. Spin physics: (A) In ordinary situations, each spin points in a random direction. (B) The spin aligns parallel or antiparallelly to an external B_0 field.

2.1.3. Radio-frequency Pulse Excitation

The spins align with the axes of the external B_0 field and create net magnetization (M_0) as they are placed in the field, but there is no signal received since the oscillating signal is the only one that we can transmit and receive [18][21]. Neither can the oscillating spins along the z-axis, which is parallel to the B_0 field, be detected [21]. To create such transmittable and receivable signals, a radio-frequency pulse (RF), which is also called an RF field (B_1), is applied. This flips the net magnetization [21]. For example, if we apply a 90° RF pulse along the x-axis, the net magnetization flips to the x-y plane from the original z-axis, as shown in Fig. 2 [15]. The flip angle

(α) obeys Eq. (2-3), which is proportional to the RF field (B_1), and to the time of duration (τ_{B1}) [15][21].

$$\alpha = \gamma B_1 \tau_{B1} \quad (2-3)$$

The flipped net magnetization then rotates around B_0 while obeying the Larmor frequency. Since the flipped net magnetization can induce a current alternation within the receiver coil, a signal can be generated [18].

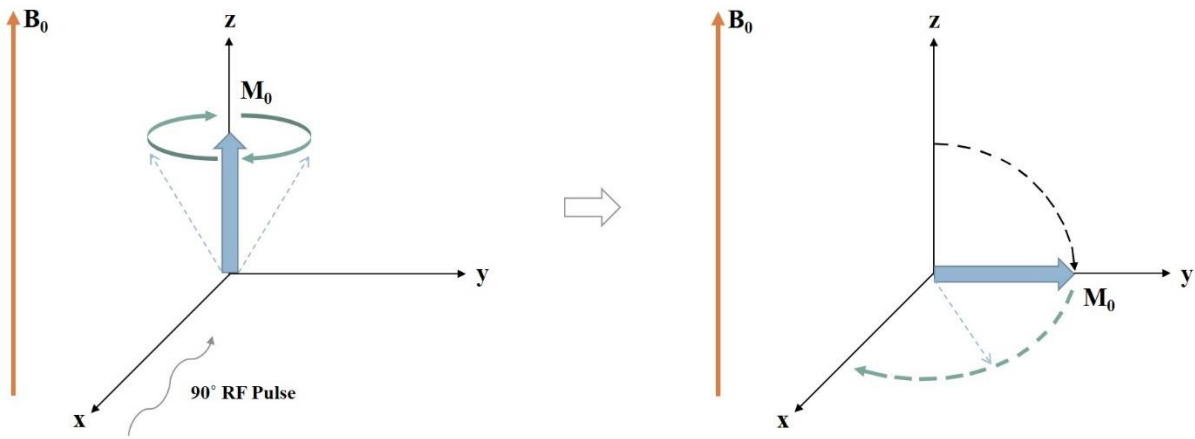


Figure 2. The spins generate a net magnetization that aligns with the external magnetic field while precessing around the z-axis. When a 90° RF pulse is applied, the net magnetization is flipped to the x-y plane and it precesses in the x-y plane.

2.1.4. Spin-lattice and Spin-spin Relaxation

The net magnetization (M_0) can be divided into M_x , M_y and M_z [15]. When spins are in their equilibrium state, M_0 is composed of merely M_z . This indicates that M_z equals M_0 , and both M_x and M_y equal zero [15]. However, when M_0 is flipped to the x-y plane by the excitation of a 90° RF field, both M_x and M_y consist the M_0 instead of M_z . When the RF field is turned off, the spins tend to relax to their lowest energy level or their equilibrium state [22].

There are two types of relaxation, spin-lattice relaxation and spin-spin relaxation, also known as T_1 -relaxation and T_2 -relaxation [15][23]. T_1 is the longitudinal relaxation time, which refers to the time it takes for M_0 to realigns with the z-axis [22]. It is also known as the time for M_z to recover from zero to 63% of its maximum value, as shown in Fig. 3 [18][23]. T_2 is the transverse relaxation time, which is associated with the dephasing of M_{xy} , after the RF field is turned off [22]. It is also the length of time for the M_{xy} to decay to 37% of maximum value from its original value, as illustrated in Fig. 3 [18][23].

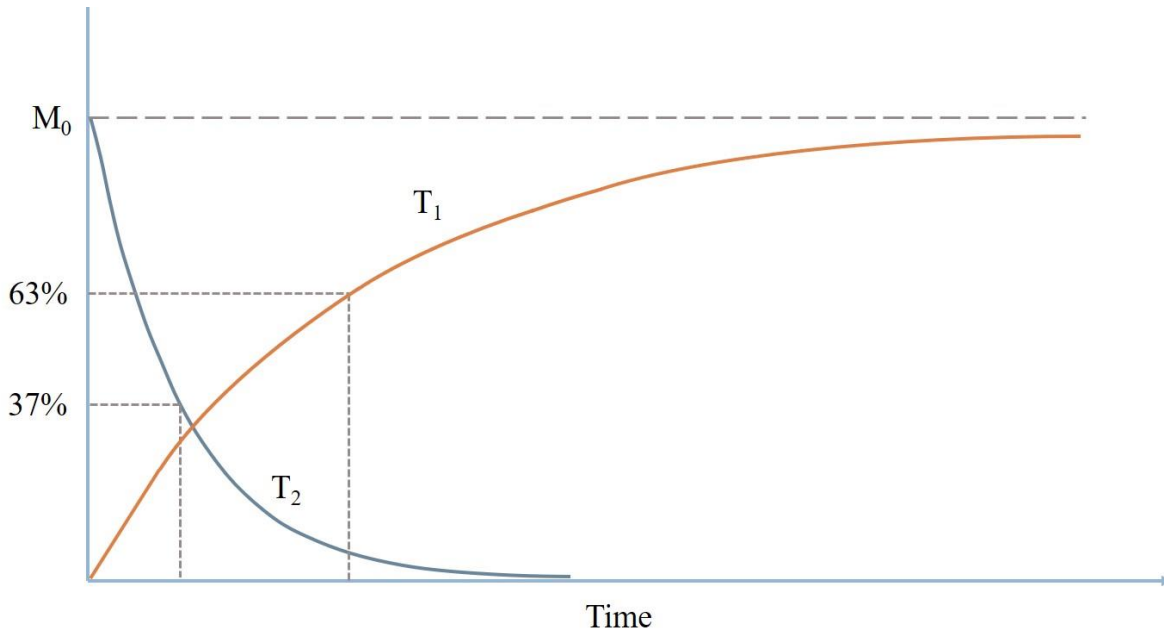


Figure 3. T_1 and T_2 relaxation: After the RF pulse is turned off, longitudinal magnetization, or T_1 relaxation, starts to recover. T_1 relaxation time is the time needed for T_1 relaxation to reach 63% of maximum magnetization. At the same time, transverse magnetization, or T_2 relaxation, starts to decay. The T_2 relaxation time is the time needed for T_2 relaxation to decay to 37% of its initial magnetization.

Both T_1 and T_2 relaxations can be described mathematically through the Bloch equations.

For T_1 relaxation, the recovery of M_z is shown in Eq. (2-4) [15]:

$$M_z(t) = M_0 \cos\alpha + (M_0 - M_0 \cos\alpha)(1 - e^{-t/T_1}) \quad (2-4)$$

For T_2 relaxation, the dephasing of M_{xy} after the RF field is turned off is given by Eq. (2-5) [15]:

$$M_{xy} = M_0 \sin\alpha(e^{-t/T_2}) \quad (2-5)$$

In general, T_2 relaxation time tends to be shorter than T_1 relaxation time [15][18]. However, T_1 relaxation time and T_2 relaxation time do not interfere with each other, and there is no correlation between them [15]. Moreover, each tissue has its own T_1 and T_2 relaxation times [18]. T_2 relaxation is driven only by the spin-spin interaction, but T_2^* is driven by both spin-spin interaction and the inhomogeneity of the external B_0 field [22][23]. The relationship between the two is given by Eq. (2-6):

$$\frac{1}{T_2^*} = \frac{1}{T_2} + \gamma \Delta B \quad (2-6)$$

where γ is the gyromagnetic ratio, and ΔB is the B_0 field inhomogeneity. It should also be noted that the T_2^* relaxation time is always shorter than the T_2 relaxation time [22].

2.1.5. Repetition Time (TR) and Time to Echo (TE)

During scanning, we apply several RF pulses, and the time between pulses is known as repetition time (TR) [24]. In the spin-echo sequence, two RF pulses are applied, of which the first is the 90° pulse followed by the 180° pulse some time later ($\frac{TE}{2}$) [18][25]. The 90° pulse flips the net magnetization to the x-y plane. Then, as the spins start dephasing, the 180° pulse makes the spins rephase [25]. The time when the spins rephase to the maximum is known as the time to echo

(TE) [14][25]. And the signal is proportional to the mobile protons $N(H)$, T_1 relaxation and T_2 or T_2^* relaxation, is shown in Eq. (2-7):

$$S \propto N(H)(1 - e^{-TR/T_1})(e^{-TE/T_2^*}) \quad (2-7)$$

2.1.6. Free Induction Decay

The MR signal is transmitted and received through electromagnetic induction, which can be detected only from the spin in the x-y plane [15][21][26]. After the RF field is turned off, the magnitude of the rotating M_{xy} around the x-y plane gradually dephases [18][22]. The decaying magnitude of M_{xy} is described by Eq. (2-8). The decaying of M_{xy} is caused by the free precessing of spins when they emit absorbed energy [22][26]. Therefore, the detected signal generated by the oscillating spins gradually decreases to zero [18][22]. This process is known as Free Induction Decay (FID) as shown in Fig. 4.

$$M_{xy}(t) = M_0 e^{-t/T_2^*} (\cos \omega_0 t) \quad (2-8)$$

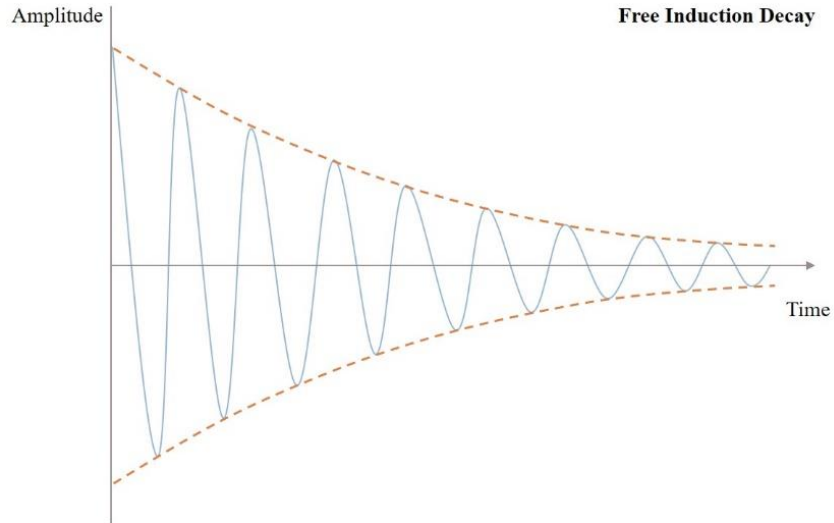


Figure 4. Free induction decay: The signal received by the receiver coil gradually decays as the spins recover to their original state, after the RF pulse is turned off.

2.2. THE ELEMENTS OF MR IMAGING

To take a photograph, we need a light source and an object that we are photographing. The object reflects the light to the photographic plate in the camera, and gives us the photograph we want [17]. Magnetic resonance imaging uses the same idea as a photograph. In MR imaging, the light source is replaced by the radio-frequency pulse (RF), and the photographic plate is replaced by the signal receiver [17]. In MRI, the RF pulse transmits into the tissue, the magnetic spin within the tissue receives the pulse and generate signals that are received by the signal receiver. Then we acquire the MR image [17].

2.2.1. T_1 , T_2 , and Proton-density Weighting Image Contrast

Every tissue has a T_1 relaxation time that is different from other tissues [15]. The same as true for a tissue's T_2 relaxation time [15]. Such characteristics allow us to acquire an MR image with excellent tissue contrast [24]. By combining different portions of TR and TE, the T_1 weighting, T_2 weighting and proton-density weighting the image is produced as shown in Table I [15][24][27].

Table I. Intervals for image weighting

Image weighting	TR	TE
T_1 weighting	Short	Short
T_2 weighting	Long	Long
Proton density weighting	Long	Short

2.2.2. Image Acquisition

There are three components involved in the acquisition of an MR image: slice selection, phase-encoding and frequency-encoding, and each of these works independently [15][28][29]. These components are carried out by gradients G_x , G_y and G_z , which depend on the orientation of

the x-axis, y-axis and z-axis, respectively [28]. The slice orientation can be axial, coronal, or sagittal, depending on the combination of G_x , G_y and G_z . That is, each gradient can be a slice-select gradient, a phase-encoding gradient, or a frequency-encoding gradient [28].

To select a slice, the slice-select gradient (G_{slice}) is applied and added to the external B_0 field. This makes the subject experience a slight variation of the magnetic field from point to point along the slice orientation axis [14][15][28][29]. As we transmit a specific RF pulse (ω_s) that corresponds to the Larmor frequency of the certain range of the subject, we excite the protons in that area so that the spins within that area experience the same magnetic field, as shown in Fig. 5 [15][28][29].

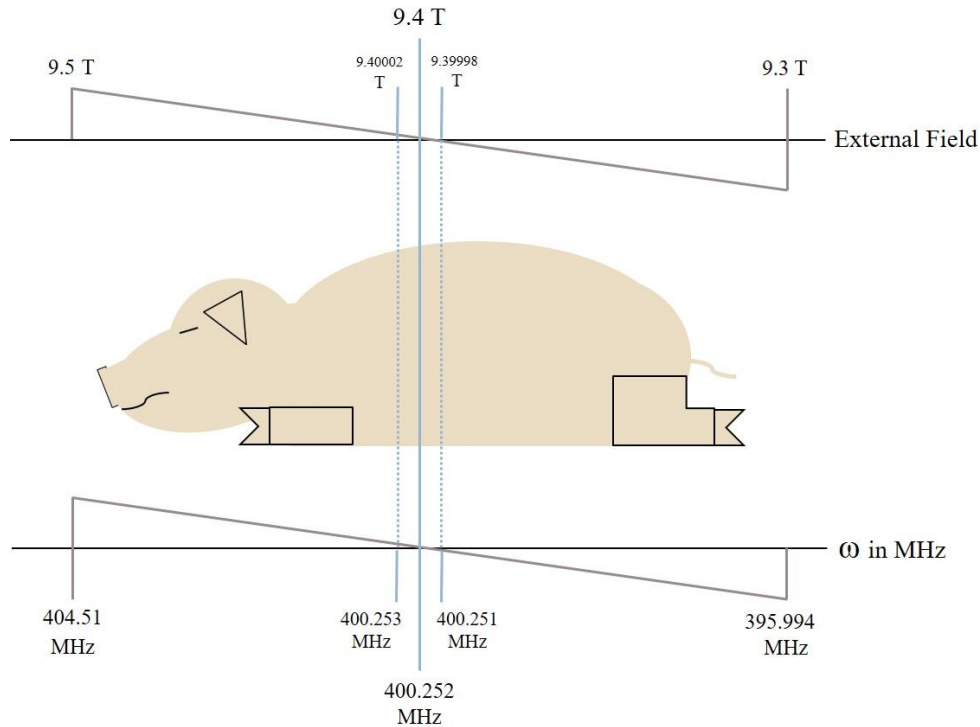


Figure 5. Slice-selection: The slice-selection gradient is used to select a specific slice of interest. The gradient creates a slightly different field along the subject. To excite a specific slice, a specific RF pulse is transmitted, which matches the spin-precessing frequency in the tissue in the slice.

The excitation bandwidth is given by Eq. (2-9) [15]:

$$Bandwidth = \omega_0 \pm \Delta\omega_s \quad (2-9)$$

The thickness of the slice is governed by the slice-selection gradient and the bandwidth of the RF pulse. By increasing the G_{slice} or decreasing the bandwidth of the RF pulse can we narrow the thickness of a slice [28].

As its name implies, the phase-encoding gradient (G_{phase}) is used to create a difference in phase between the grids that compose the image, as shown in Fig. 6 [30].

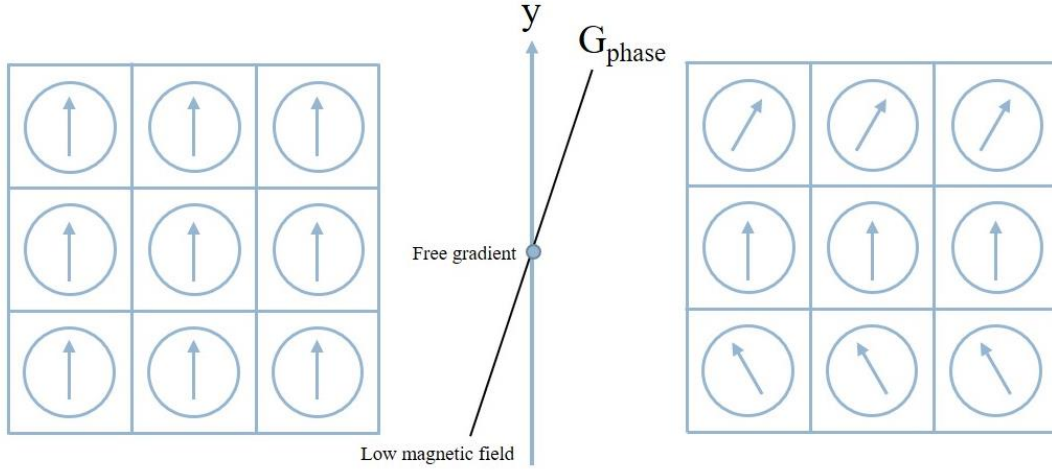


Figure 6. The phase-encoding gradient: By applying a phase gradient along the y axis (as in this example), the spins of the lines experience different magnetic fields and precess differently according to the field.

If we apply a G_{phase} along the y axis, the net phase shift is given by Eq. (2-10) [15]:

$$\varphi = \gamma G_y y \cdot \tau \quad (2-10)$$

where φ is the phase shift and τ is the duration of time.

In a similar manner, the frequency-encoding gradient (G_{freq}) is used to create differences in frequency from position to position, as illustrated in Fig. 7 [30].

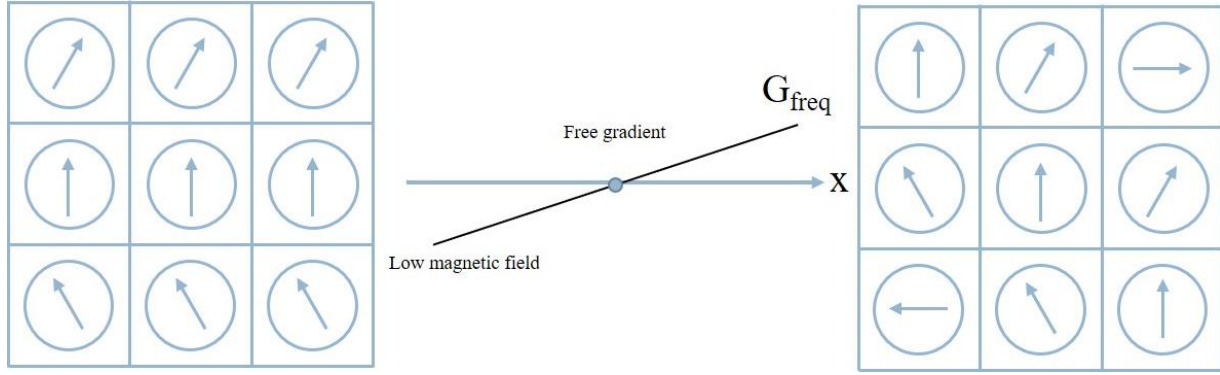


Figure 7. The frequency-encoding gradient: After applying the phase-encoding gradient along the y-axis, the frequency-encoding gradient is applied along the x-axis. As a result, the spin in each grid precesses differently.

The spatial information is given by Eq. (2-11), which depends on the positions of the protons [15]:

$$\omega_x = \omega_0 + \gamma G_x x \quad (2-11)$$

Where the x is the location of the protons.

Both G_{phase} and G_{freq} are used to differentiate individual grids an image, as illustrated in Fig. 6 and 7 [18], but phase-encoding gradient is always applied before the frequency-encoding gradient [30]. Therefore, the protons in each grid can be distinguished in terms of both phase and frequency [30]. The signal receiver is gated on when G_{freq} is applied, which it is also called the readout gradient [15][30].

The spatial information is filled into the k-space with the value of the frequencies [15]. When the k-space is filled, we do a Fourier transform (FT). Then we can reconstruct the MR image [15][31][32].

2.2.3. Fast Spin Echo Sequence

Compared to the conventional spin-echo (CSE) sequence, the fast-spin echo (FSE) sequence is less time consuming [33]. In the CSE sequence, there is a single phase-encoding step in a TR. That is, we obtain an echo only after applying the phase-encoding gradient [33]. Each echo obtained has its own k-space line, and each line of k-space generates one image [33]. And the time cost to acquire the target image is given by Eq. 2-12 [33]:

$$\text{Scan time (CSE)} = TR \cdot (\text{number of phase - encoding steps}) \cdot NEX \quad (2-12)$$

where NEX is the number of excitations.

However, the FSE sequence is achieved by modifying the CSE sequence to save time. With FSE, there are multiple phase-encoding steps in one TR, so that we get multiple echoes at once [33]. Instead of filling these signals into separate k-space, we fill them into one k-space [33]. The signals generated from the next TR also are filled into the same k-space. The time cost is shown in Eq. 2-13 [33]. By doing this we can save time comparing to the CSE when we are acquiring MR image [33]:

$$\text{Scan time (FSE)} = (TR \cdot (\text{number of phase - encoding steps}) \cdot NEX) / ETL \quad (2-13)$$

where ETL is the echo train length.

2.2.4. Three-dimensional Imaging

A typical two-dimensional MR image is acquired by applying G_{slice} , G_{phase} , and G_{freq} along with the three orientations one at a time, respectively [15][28]. On the other hand, a three-dimensional MRI is performed if we apply the G_{phase} along two axes at the same time [33][34]. This makes a pixel become volume and a slice become a slab. As techniques and equipment have improved, three-dimensional FSE imaging is possible [33][34]. The scanning time for the axial view of the 3D FSE image is given by Eq. (2-12) [33]:

$$3D \text{ FSE scan time} = (TR \cdot NEX \cdot N_y \cdot N_z) / ETL \quad (2-14)$$

where N_y and N_z are phase-encoding steps along the relative axes [33].

3. BRAIN DEVELOPMENT

3.1. THE BRAIN IN GENERAL

The central neural system connects the whole body through the brain stem and the spinal cord [35]. The largest part of the brain is the cerebrum which has the two cerebral cortexes connected by the corpus callosum [35]. Each cortex can be divided into four lobes: the frontal, the parietal, the temporal and the occipital lobes [35]. Other structures under the cerebral cortex such as the thalamus, the hypothalamus, the hippocampus, the putamen, the caudate nucleus, and the olfactory bulb also are part of the cerebrum [35]. The brain stem consists of three structures, the midbrain, the pons, and the medulla [35]. On the other hand, from the perspective of its development, the brain can be divided into three parts: the forebrain, the midbrain and the hindbrain [36][37]. In this perspective, the pons, the medulla and the cerebellum belong to the hindbrain, while the others remain the same [36][37]. Overall, the brain is an important organ that deals with the thoughts, actions, desires and cognition of the human being [35].

The cognitive function is executed in the cerebral cortex, one of the most important structures of the central neural system [38]. The cerebral cortex is a laminar tissue, of which the upper part contains the neurons and the lower parts are the connecting neurons, which link with the other parts of the brain [39]. The cerebral cortex is equipped with neural circuitry, which consists of neurons and fibers, that performs the computation of cognition involving the sensory and motor functions [38][40]. The Purkinje cell and the granule cells are the two major neural cells that constitute the cerebellum [41]. It has long been known that the cerebellum controls movement and balance [42]. However, the role of the cerebellum involves much more than motion: it has cognitive functions, such as sensory-motor learning and spatial memory [43]. The three components of the brainstem, from top to bottom, are the midbrain, the pons, and the medulla

[44][45]. One of the important roles of the brainstem is to transmit information between the cerebrum, the cerebellum and the spinal cord [45]. Another critical task of the brainstem is the autonomic control of the body [46]. The midbrain is associated with stress and pain responses, respiration control, and micturition coordination [46]. The superior and inferior colliculi of the midbrain relate to the visual system and the auditory system, respectively [44]. The gastrointestinal, respiratory and cardiovascular functions are controlled autonomically by the pons [46]. The relaying center for taste is in the medulla, which is involved in several autonomic reflexes as well. These including the cardiac and baroreflex, carotid chemoreflex, and pulmonary mechanoreceptor reflex [46]. The medulla is also associated with the sensation of the viscera, the motility of the gastrointestinal tract and the control of blood pressure [46].

The thalamus is the major structure of the diencephalon, which links the cerebral cortex with the other subcortical structures [47]. The character of the thalamus as a gateway involves it in several neurologic functions such as motion, the senses and integration [47]. It also involves physical regulations, including sleep and wakefulness, memory, emotion, consciousness, awareness and attention [47]. In the inferior of the thalamus, there is the subthalamus [44]. Both globus pallidus and substantia nigra are linked with the subthalamic nucleus, which involves it in the movement control [44]. The odor information is received by the olfactory bulb from the olfactory sensory neurons, which lie in the olfactory epithelium in the nose [48]. The olfactory bulb does primary processing and then passes the signal to the piriform cortex, where the information is processed again and sent to higher-level regions in the brain [48].

The hippocampus is an extensive structure outside the temporal lobe of the cerebral cortex, but it is quite different from the cerebral cortex from the functional, anatomical and cytoarchitectural points of view [49]. It is an important structure that not only relates to memory

and learning but also associates with spatial recognition and emotional behavior [49][50][51]. The putamen and the caudate nucleus share similar histology [52], and the two can be combined to form striatum [53]. The putamen helps make motor movements smooth [52], and it is also associated with learning and memory functions from the stimulus [54]. Unlike the putamen, the caudate nucleus is involved in higher-level cognitive functions such as learning, memory, execution and social communication [53]. The corpus callosum contains millions of neural axons, which makes it the greatest white matter structure within the brain [37][55]. Its function is to connect the right and the left cerebral hemispheres so that they can communicate [37][55].

The major responsibility of the pituitary gland is to regulate the body's endocrine system [56]. This gland comprises the anterior lobe, the intermediate lobe and the posterior lobe [56]. Each lobe secretes several endocrine hormones. The anterior lobe produces six hormones: the growth hormone (GH), the luteinizing hormone (LH), the follicle-stimulating hormone (FSH), the thyroid-stimulating hormone (TSH), the adrenocorticotrophin (ACTH) and prolactin (PRL). The intermediate lobe produces one hormone, the melanocyte-stimulating hormone (MSH). Oxytocin (OXT) and the antidiuretic hormone (ADH) are produced by the posterior lobe [56]. The pineal gland is a structure developed from the forebrain that produces and secretes melatonin, an indole compound, in the brain [57][58]. That hormone is involved in numerous functions within the body. For instance, it controls the circadian rhythms, is involved in antioxidant defense and performs immune responses [58]. The spinal cord belongs to the central nervous system that delivers the signal between the brain and the body [37][46]. The spinal cord has thirty-one segments that connect the brain with the upper limb and the lower limb [37][46].

3.2. HUMAN BRAIN DEVELOPMENT AND INTELLIGENCE

The human brain begins to develop in the third week of gestation [59]. The volume of the human brain increase approximately fourfold from birth to the teenage years [59][60]. The growth of the brain after birth [61] includes four periods of rapid growth or “spurts.” They occur at ages 2~4, 5~8, 10~13 and 15~18 [62]. Although the brain grows differently in males and females, and the female brain mature earlier, both reflect the main periods of rapid growth [62]. On the other hand, the growth of the brain after the first period is difficult to associate with a single factor [62]. Epstein pointed out that both nutritional adequation and sociocultural sufficiency trigger the growth of the brain [62]. Moreover, a study of infant’s brains showed that the volume of the total brain increased rapidly within 90 days after birth and exhibited a growth rate of 64% [63]. However, the structures of the brain do not grow equally [60]. The cerebellum exhibits rapid growth during the early period of development [61], it can double in volume in the first 90 days after birth [63]. By contrast, the hippocampus increases only 47% during that period [63]. Holland found that the neonatal brain was asymmetrical; some left brain structures were larger than those on the right and vice versa [63]. Even within the same structure, the growth rate of each part is different [60]. Simmonds’s study showed that the hippocampus continued to develop throughout childhood by increasing its synaptic density and myelination [64]. However, synaptic density is not always increasing; it can be reversed [60]. The number of neurons in the human brain is the same at birth and in adulthood [65], and most of the neurons in the brain have migrated to their proper locations by the time the fetus is born [60].

Although the number of neuron cells in the brain nearly stops increasing at birth, the volume of the brain still grows, and while neurogenesis stops in most of the brain at birth, it does continue in the hippocampus through adulthood [60]. This means that the neurons in the brain

become larger and their dendrite become more complex, so that brain volume grows even though the number of neurons does not increase [41][44][47]. The development of the brain after birth is associated with the growth of neurons, and it is accompanied by the formation of synapses and the myelination of neural fibers [60].

In humans, the overall size of the brain, cortical thickness and the volume of gray matter are associated with a high intelligence quotient (IQ) score [48][50][67], and the complexity of the cerebral cortical region is associated with cognitive ability [67][68]. The complexity of neuron dendrite and the size of the neurons also correlate with higher intelligence [66].

3.3. ANIMAL MODELS FOR BRAIN RESEARCH

Dobbing has shown that the human brain has a development pattern that is different from that of other primates. The weight gain of the brains of other primates reaches its peak before birth. On the other hand, the growth of a pig's brain has a peak at birth like those in human brains, although they do not have the same pattern. Moreover, the ratio of the adult brain to the infant brain at birth is similar between humans and pigs [69]. Jelsing's study has shown that the number of neurons in the brain of domestic piglet is nearly fixed at birth, which has the same result as the human brain does [65]. The brain atlas of the rodent model has been well established; however, it is a small animal model that cannot fully link to the human brain. Therefore, we need a large animal model that is more closely related to humans to mimic the real pathologies in patients [16]. These make the pig brain an ideal model to study brain development and related research.

3.4. PIGLET BRAIN

Based on brain weight data, some have concluded that the growth spurt of the piglet brain starts about 50 days before birth and lasts approximately 40 days after birth. During this period,

the piglet brain grows rapidly, increasing as much as 6% of the weight of the mature brain. Besides the growth of the whole brain, the growth of the cerebellum is interesting. It can grow faster than the other parts of the brain and reach as much as 11% of the weight of the mature brain at birth. The compositions within the brain change while the brain gains weight. The amount of water decreases while cholesterol, which is representative of lipid, increases as the brain grows in weight [70].

On the other hand, the data on volume collected from MRI shows that the most rapid growth of the whole brain occurs from the age of 4 weeks to 12 weeks. Compared to humans, whose right hippocampus is slightly larger than the left hippocampus, the left and the right hippocampus of the piglet seem to be the same. In addition, the developing patterns of the diencephalon (which comprises the thalamus, the subthalamus, the pituitary gland, and the pineal gland) and the brain stem (which comprises of the midbrain, the pons and the medulla) are similar in piglets and humans [5]. Pigs can learn and remember, which makes them a good model for cognition research [6][51].

Radlowski found that small born gestational-age piglets display poorer cognition than average born gestational-age piglets. Although the volume of the whole brain and most of the brain structures of the small born gestational-age piglet and the average born gestational-age piglet are not significant difference, the gray matter volume of the brain of a small, born, gestational-age piglet is considerably less than the other [71].

4. EVALUATION OF PIGLET BRAIN STRUCTURES WITH *EX VIVO* IMAGES

4.1. INTRODUCTION

Early brain development is crucial, for it can profoundly affect the rest of life. However, the trajectories of brain development in fetuses and infants are still ambiguous [5][55] [63][72]. Several difficulties exist in acquiring data about the brain development patterns of the fetus and the infant. For one thing, inadequate imaging techniques made it hard to obtain the image of the brain under the skull in the past. Unlike with animal models, it is arduous to acquire fixed images of the fetus and the infant [72], which can lead to poor image quality [63]. Ethical issues are another factor that has affected the few studies performed directly on the fetus or the infant brain [5][69]. These difficulties make the animal model an irreplaceable resource for studying brain development. To date, most knowledge about early brain development patterns comes from animal models, and most of it comes from the rodent brains [9][73]. However, it was reported that the porcine brain has a pattern similar to that of humans [69], which makes the pig a feasible animal model [74]. The use of pigs for preclinical research, such as experimental surgery and physiological study, has been well established [75]. Nevertheless, the knowledge of the pig brain is still deficient and the data is still being collected [7][76]. Because of inadequate brain investigating techniques, measuring the circumference of the head [62] or weighing the brain [69] became strategies for studying brain development in the past. However, when the magnetic resonance imaging (MRI) was introduced to the neuroscience field, it became a dominant clinical modality for studying the brain [14].

Using MRI for investigating the brain has several benefits. First, compared to imaging that requires radiation such as X-ray radiography and Positron emission tomography (PET), MR imaging is ionizing radiation-free, and it can be performed noninvasively [14][15][18]. Unlike X-

ray radiography and PET, excellent soft-tissue contrast can be achieved through MRI [14][15]. The image acquired from MRI is flexible; both two-dimensional and three-dimensional images are available [15][16]. Besides, MRI can provide high spatial resolution. It can acquire a high-resolution image with sub-millimeter orders, depending on which types of images are acquired [15][16]. These characteristics allow us to obtain details about the anatomy of the brain without damaging it. This makes MRI an ideal modality for brain research.

The investigation of pig brain structures have already been performed with MRI [77]. The MRI pig brain atlas contains data sets of Göttingen minipig brains reconstructed at the age of 10 months on average. The images were acquired with a 1T MR scanner [7]. Moreover, three-dimensional high-resolution MR images of six-month-old female domestic pigs were acquired with a 4.7T scanner [78]. Other sets of five-month-old pigs were acquired with a 1T scanner. In that case, instead of doing structural segmentation, the position of structures were labeled [79]. Another study of pig brains was performed at the neonatal age of 28 days using a 3T MR scanner with an isotropic voxel size of 0.7 mm [71]. The brains of younger domestic piglets at the age of 2 to 5 weeks [80] and 2 to 24 weeks [5] were evaluated with the help of a 3T MR scanner. However, only five brain structures—the cerebral cortex, the cerebellum, the brainstem, the diencephalon and the hippocampus—and the total brain volume were evaluated [5][80]. Despite all the material in the database about the porcine brain, there is a lack of data on the piglet brain with detailed segmentation of brain structures that shows the neonatal piglet brain anatomy reconstructed from high-resolution MRI performed with an ultra-high-field MR scanner.

Therefore, we would like to investigate neonatal piglet brains from three-dimensional high-resolution MR images acquired from a 9.4T ultrahigh-field MR scanner at the age of 12 days. A total of 15 piglet brain structures were manually segmented and evaluated in this study.

4.2. MATERIAL AND METHODS

4.2.1. Specimen preparation

The brains of 19 piglet at the age of 12 days were harvested with skull for volume evaluations after those piglets were sacrificed (approved by Institutional Animal Care and Use Committee, number: 18-046). The dissected heads were rapid frozen in liquid nitrogen and stored in the -80 °C freezer to keep fresh. Each subject was moved from the -80 °C freezer to the -20 °C freezer before it was scheduled for scanning. The subject was thawed at 4 °C for 22 to 24 hours to allow the ice to dissolve and prepare the brain for scanning.

4.2.2. MRI acquisition

Ex vivo images, of all the brains were acquired with a 9.4T MRI scanner (Agilent, Santa Clara, CA) and 72 mm ID birdcage volume RF coil (Rapid, Germany). The high-resolution scan was a T₂-weighted 3-dimensional fast spin echo sequence. The imaging parameters were: TR = 1500.00 ms, TE = 46.00 ms, Echo space (ESP) = 6.58 ms, segments/echo train length (ETL) = 16/16, k_{zero} = 7, average = 1, field of view = 90 × 65 × 65 mm³, data matrix = 384 × 256 × 256, slab thickness = 65 and spatial resolution—0.2344 × 0.2539 × 0.2539 mm³. The total scanning time for each 3-dimensional T₂-weighted image was 1 hour 42 minutes and 27 seconds.

4.2.3. Delineation and segmentation

Because there is no piglet brain atlas at the age of 12 days, several references were used to assist in the identification and segmentation of the piglet brain structures. These included studies by Conrad works [5][80], Lind [6], Watanabe [7], Fabris [8], Fe'lix [76], Yun [77], Saikali [78] and Schmidt [79]. To identify each structure as precisely as possible, the boundaries of the structures in the coronal, the sagittal and the axial views were considered at the same time. In

addition, the position relative to the references was noted. These brains were processed one at a time to establish references for the brain images obtained later.

4.2.4. Analysis of the volumes of the structures

Each brain structure was reconstructed using ITK-SNAP software, and its volume was calculated as shown in Eq. (4-1):

$$Volume = Number\ of\ voxels\ segmented \times Voxel\ size \quad (4-1)$$

The total brain volume was obtained by adding all the segmented structures except the spinal cord. The mean volume of each brain structure was obtained by averaging the volumes of the 19 instances of each structure. The percentage of each structure was obtained as shown in Eq. (4-2).

$$Percentage\ (\%) = \left(\frac{Mean\ structural\ volume}{Mean\ total\ brain\ volume} \right) \times 100 \quad (4-2)$$

The volume was express as mean \pm standard deviation. All the statistical analyses were calculated using SPSS software (Version 27, IBM, Chicago), and the figures were made with Excel (Microsoft Office 365, Microsoft, WA).

4.3. RESULTS

4.3.1. Piglet brain segmentation

Images of segmentation from three angles of view of the piglet brain are shown in Fig. 8. The original image of coronal view before segmentation is shown in Fig. 8 (A). The raw axial image is shown in Fig. 8 (B). And the raw sagittal image is shown is Fig. 8 (C). Fig. 8 (G) shows the labels for each segmented structure. Eight structures are shown in the coronal view Fig. 8 (D): the cerebral cortex; the cerebellum, which is at the bottom of the image and in the posterior of the

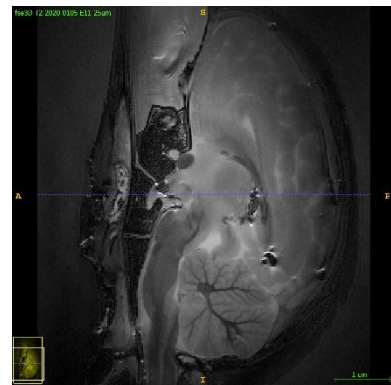
piglet brain; the thalamus, which is in the middle of the brain and the image; the midbrain, which is beneath the thalamus; the olfactory bulb, which is at the top of the image and in the anterior of the piglet brain; the hippocampus, which is next to the thalamus; the putamen, which is above the thalamus; and the caudate nucleus, which is beside the putamen. In the axial view— Fig. 8 (E)— there are eight structures, and all the structures are presented upside down. This image is taken from the middle part of the piglet brain along the front and back trail of the head. The segmented are the cerebral cortex, the midbrain, the thalamus, the subthalamus, the hippocampus, the putamen, the caudate nucleus and the corpus callosum. The sagittal view of the piglet brain is shown in Fig. 8 (F). It has 12 segmented structures: the cerebral cortex, the cerebellum, the midbrain, the medulla, the pons, the thalamus, the subthalamus, the olfactory bulb, the corpus callosum, the pituitary gland, the pineal gland and the spinal cord.



(A)



(B)



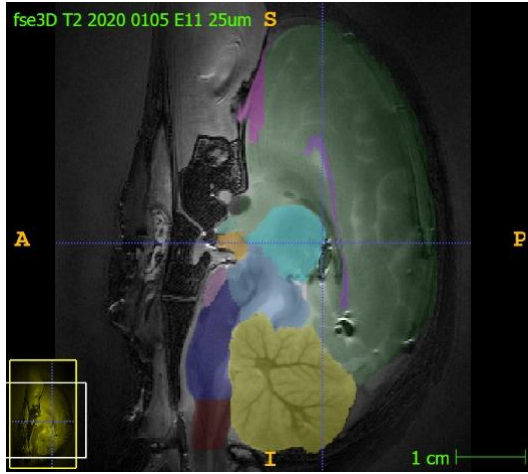
(C)



(D)



(E)



(F)

1	Cerebellum	9	Pineal gland
2	Cerebral cortex	10	Pituitary gland
3	Corpus callosum	11	Pons
4	Caudate nucleus	12	Putamen
5	Hippocampus	13	Subthalamus
6	Midbrain	14	Spinal cord
7	Medulla	15	Thalamus
8	Olfactory bulb		

(G)

Figure 8. High-resolution images of 15 segmented structures of the piglet brain. (A) The raw image of coronal view. (B) The raw image of axial view. (C) The raw image of sagittal view. (D) The coronal view after segmentation. (E) The axial view after segmentation. (F) The sagittal view after segmentation. (G) Segmentation labels.

The three-dimensional models reconstructed from the segmentation images of the piglet brain are shown in Fig. 9. The original images without segmentation are shown in Fig. 8 (A), (B), (C). Fig. 9 (A) is the view from the left and the right axis, and Fig. 9 (B) is the view from the

superior and inferior axis. There are 15 structures included in these models, and the labels of the structures are the same as in Fig. 8 (G). Most of the piglet brain structures are evident in these three-dimensional models.

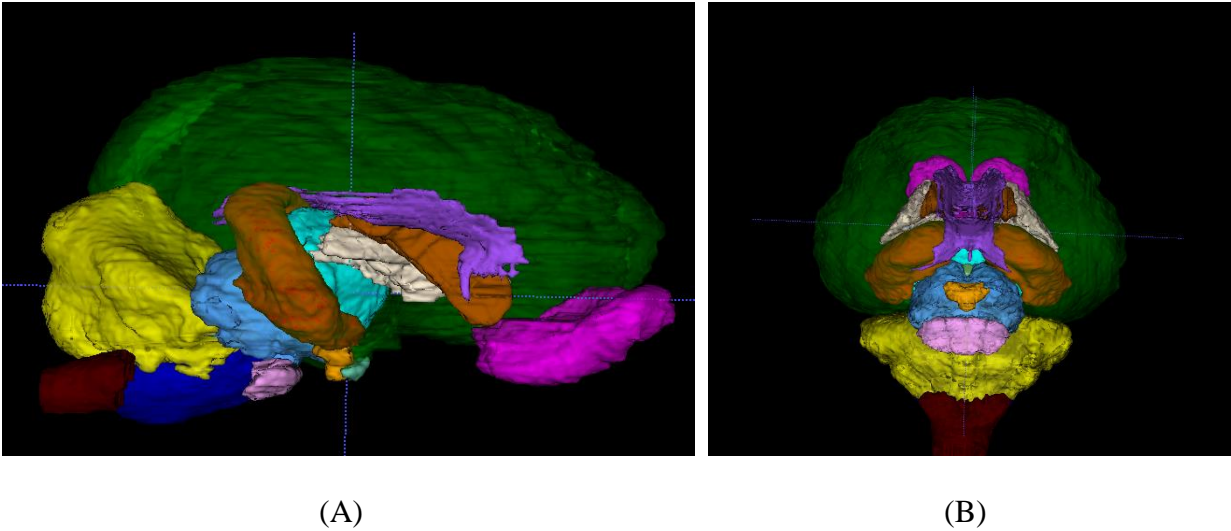


Figure 9. The three-dimensional model of the piglet brain reconstructed from three-dimensional T_2 -weighted images: (A) The left-right view. (B) The superior-inferior view.

To get a closer view of each structure, we isolated it from the three-dimensional model as shown in Fig. 10. As we can see, each structure has its own shape in the piglet brain, while the relative size of each structure can be seen in Fig. 9.

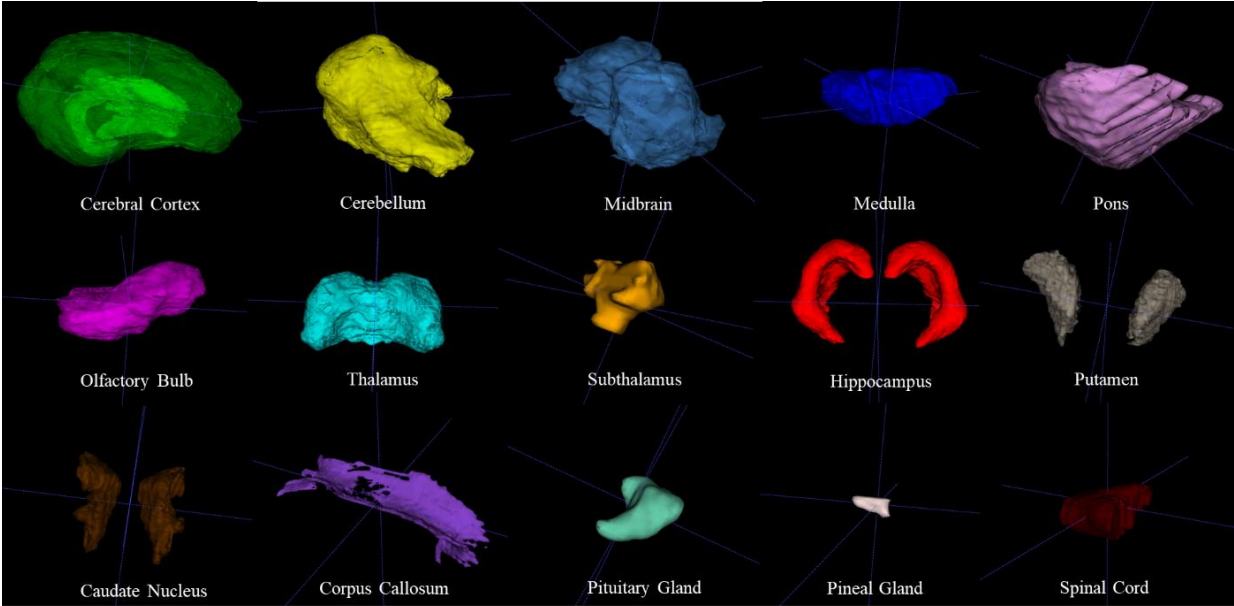


Figure 10. Illustrations of 15 segmented structures of the piglet brain.

4.3.2. Volumetric analysis

The volume of each piglet brain structure is shown in Fig. 11. On average, the cerebral cortex was the largest structure, at about $27.366 \pm 1.879 \text{ cm}^3$, followed by the cerebellum at $4.204 \pm 0.454 \text{ cm}^3$ which also was large. The brain stem, which contained the midbrain, pons, and medulla, was third at $3.090 \pm 0.313 \text{ cm}^3$ total volume. The volumes of each brain stem three brain stem structures were $1.512 \pm 0.095 \text{ cm}^3$, $1.208 \pm 0.157 \text{ cm}^3$ and $0.371 \pm 0.061 \text{ cm}^3$, respectively. The thalamus and the olfactory bulb also were big structures in the piglet brain. Their average volumes were $1.484 \pm 0.114 \text{ cm}^3$ and $1.410 \pm 0.199 \text{ cm}^3$.

The mean volume of the hippocampus in the high-resolution images was $0.847 \pm 0.074 \text{ cm}^3$. The volumes of the putamen, the caudate nucleus, and the corpus callosum were approximately $0.714 \pm 0.061 \text{ cm}^3$, $0.458 \pm 0.050 \text{ cm}^3$ and $0.168 \pm 0.030 \text{ cm}^3$, respectively. The subthalamus, the pituitary gland, and the pineal gland were much smaller than the other structures; their volumes were $0.043 \pm 0.006 \text{ cm}^3$, $0.021 \pm 0.004 \text{ cm}^3$ and $0.004 \pm 0.001 \text{ cm}^3$, respectively.

The spinal cord was not part of the structure of the brain, but it had a mean volume of $0.243 \pm 0.123 \text{ cm}^3$.

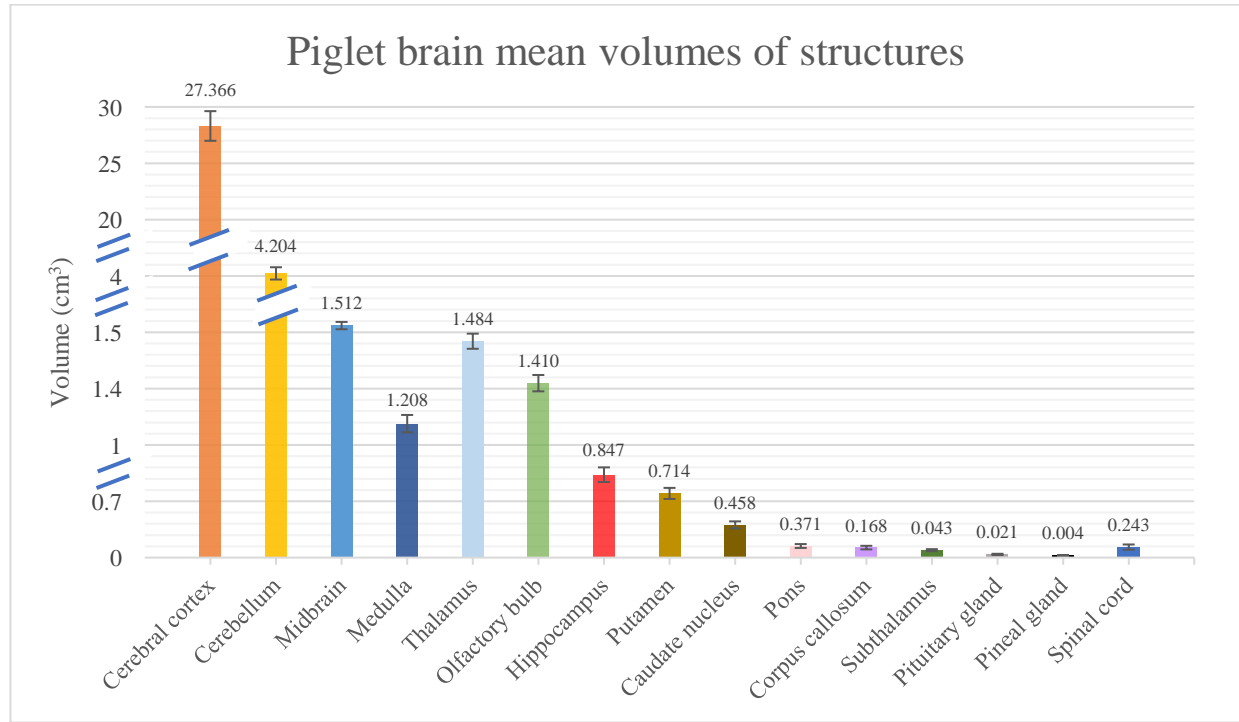


Figure 11. Mean volumes of 15 structures of the piglet brain.

Table II presents the standard deviations and the coefficient of variation of each piglet brain structures. The range of the volumes of the structures can be obtained by deducing the minimum volume of structure from the maximum volume of structure. The results showed that there were larger innate brain structures for some piglets. Most of the structures had a coefficient of variation around 12%. The small-volume structures (those with a mean volume under 0.170 cm^3) tended to have high coefficients of variation. The corpus callosum, pituitary gland, and the pineal gland had coefficients of variation around $21 \pm 5\%$. Of all the segmented structures, the spinal cord had the largest coefficient of variation at about 50%. This was because the cutting sites were different when we separated the head from the body. Noticeably, the midbrain had the smallest coefficient of variation, at about 6.3%, followed by the cerebral cortex with a coefficient of variation around

6.9%. Despite the range of coefficients for the individual structure, the coefficient of variation of the whole brain was about 6% (5.94%) when we excluded the spinal cord.

Table II. Statistics of piglet brain structures

Structure	Mean volume (cm ³)	Maximum volume (cm ³)	Minimum volume (cm ³)	Standard deviation (cm ³)	Coefficient of variation (%)
Cerebral cortex	27.366	30.361	23.843	1.879	6.87
Cerebellum	4.204	5.019	3.526	0.454	10.81
Midbrain	1.512	1.705	1.374	0.095	6.29
Medulla	1.208	1.523	1.012	0.157	12.99
Pons	0.371	0.484	0.276	0.061	16.49
Thalamus	1.484	1.705	1.294	0.114	7.71
Subthalamus	0.043	0.054	0.034	0.006	13.78
Olfactory bulb	1.410	1.835	1.116	0.199	14.09
Hippocampus	0.847	1.037	0.752	0.074	8.79
Putamen	0.714	0.808	0.618	0.061	8.61
Caudate nucleus	0.458	0.533	0.376	0.050	10.94
Corpus callosum	0.168	0.225	0.115	0.030	17.77
Pituitary gland	0.021	0.027	0.013	0.004	19.16
Pineal gland	0.004	0.005	0.002	0.001	26.71
Spinal cord	0.243	0.545	0.108	0.123	50.73
Whole brain (excludes spinal cord)	39.809	43.708	35.018	2.366	5.94

The mean percentages of the individual brain structures are shown in Fig. 12. The major structures in the brain were the cerebrum, the cerebellum, and the brain stem (including midbrain, pons, and medulla) which contributed about 68.75%, 10.57% and 7.78% to the piglet brain, respectively. The other structures contributed approximately 12.9% of the piglet brain. Those structures were the thalamus, the olfactory bulb, the hippocampus, the putamen, and the caudate nucleus, which contributed about 3.73%, 3.55%, 2.13%, 1.8% and 1.16%, respectively. The corpus callosum, the subthalamus, the pituitary gland, and the pineal gland contributed only about 0.6% of the piglet brain.

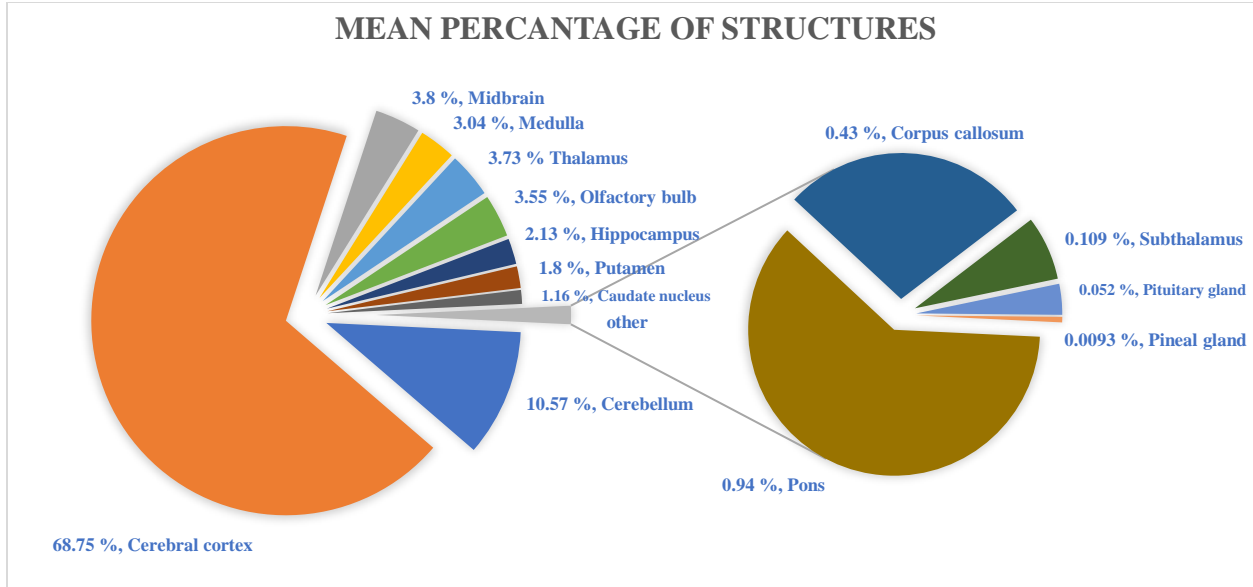


Figure 12. The percentages of the structures of the piglet brain.

4.4. DISCUSSION

In this study, we not only acquired high-resolution piglet brain MR images with a 9.4T scanner, but we also investigated the volumes of 15 structures of a neonatal piglet brain at the age of 12 days. At the same time, we constructed a database of piglet brains that included the volumes of brain structures from 19 piglets. This is the first measurement and documentation of brain structures on neonatal piglets at 12-day-old using high resolution MR images acquired by using an ultrahigh-field of 9.4T MR scanner.

Table III. Findings between Conrad's work and our data.

Structure	Our data (12 days)		Conrad's work (14 days)	
	Mean volume (cm ³)	Standard deviation (cm ³)	Mean volume (cm ³)	Standard deviation (cm ³)
Whole brain	39.809	2.366	46.162	0.642
Cerebral cortex	27.366	1.879	32.636	0.736
Cerebellum	4.204	0.454	3.919	0.069
Diencephalon	1.522	0.125	5.118	0.085
Brain stem	3.090	0.313	3.422	0.062
Hippocampus	0.847	0.074	1.066	0.042

To reconstruct the piglet brain and get a general view of its structures, we acquired high-resolution MR images and segmented the structures. A high-resolution image is much clearer than a low-resolution image [81] because the boundary of each brain structure is more easily distinguished. For the first objective of this study, 19 piglet brains were scanned at resolution of $0.2344 \times 0.2539 \times 0.2539$ mm. The high-resolution MR images made it possible for us to segment and analyze 15 brain structures in the piglet brain. Table II shows the statistics for each structure of the piglet brain. And the comparison between our findings and Conrad's study is shown in Table III. There was no doubt that the cerebral cortex was the largest structure of the brain; it contributed to nearly 70% of whole-brain volume. Conrad measured the volume of the cortex as 32.636 ± 0.736 cm³ for piglets at the age of 2 weeks [80], which is 5.27 cm³ larger than that in our finding. In our study, nearly 90% of the piglet brain was composed of the cerebral cortex, the cerebellum, and the brain stem, the three largest structures in the piglet brain. In our study, the cerebellum was 0.285 cm³ larger and the brainstem was 0.332 cm³ smaller than those of Conrad's measurements [80]. The diencephalon, which is made up of the thalamus, subthalamus, pituitary gland, and pineal gland [82], constituted about 3.9% of the piglet brain. Our measurements showed a diencephalon of 1.551 cm³, while Conrad reported 5.118 cm³ [80]. This is a large difference, which most likely is due to the lack of agreement for the boundary of diencephalon between studies. There is rare information of this structure of neonatal domestic piglets, but report from Watanabe's study shows that the diencephalon of the 10-month-old Göttingen minipig is about 2.490 ± 0.460 cm³ (5.34% of total brain) [7]. In addition, this structure is relatively small in the adult human brain with proportion of the total brain at 4% [83]. Combining the studies of Göttingen minipig report and the proportion of human brain, our measurement of 3.9% of diencephalon to the total brain is reliable compared to 11.09% in Conrad's finding. As for the hippocampus, its volume was 0.847

cm³ in our study and 1.066 cm³ in Conrad's study [80]. Although we found that the hippocampus contributed only 2.13% to the volume of the brain, it is an important structure because it is one of the major structures that relate to the ability to remember [84]. Last, total brain volume showed a 6.353 cm³ difference between our measurement and Conrad's study [80], of which our measurement was smaller. Our findings for the volumes of the cerebellum, the brainstem and the hippocampus were relatively close to those reported by Conrad. As noted earlier, there were several experimental differences between the studies. The disparities could be caused by differences in the voxel sizes of the images, difference in the image weighting form, the differences in the field strength or the differences in the conditions of subjects (the living subjects comparing to the postmortem subjects).

The size of the olfactory bulb at this age was 1.410 ± 0.199 cm³, which was close to the size of the thalamus (1.484 ± 0.114 cm³). Besides, the function of this structure is to serve as the primary processing center for the information about odor, which is an important sensory tissue within the brain [40]. Having large olfactory bulb in volume may indicate that this tissue is important in the early stage of brain development of piglet brain. The function of the corpus callosum is to connect the left and the right cerebral hemispheres [47], and it contributes merely 0.43% to the brain. This might indicate that the linkage between the two cerebral hemispheres was not fully established at this age compared to Radlowski's work (0.998 cm³ for born average gestational age piglets). In addition, we found that the whole brain volume obtained by adding the means of the brain structures did not match the mean total volume of the brain we measured from each piglet. This also is similar to Radlowski's study [71]. Most of the brain structures had coefficients of variation (CV) between 10% and 20%, and the CV for the whole brain was 5.94%,

which is the lowest of all values. This indicates that each brain structure within each piglet does not develop equally, but the development of the total brain volume may remain consistent.

The change of the total brain volume is often linked with the variance of neuron density and the volume of brain parts. However, no close relationship has been established [85]. Various factors are involved in the development of the brain. For one thing, there are limited neural stem cells, so that the development of the brain relates to the extensive proliferation and the migration of neurons [86]. Nearly 69% of the piglet brain was composed of the cerebral cortex in our study. We may think that the structure develops equally, but the surface of the cerebral cortex can be divided into different functional areas that expand heterogeneously [84]. Besides, the cerebral cortex increases by folding and buckling in the surface rather than increasing in thickness during brain development [39]. The brain development is a longitudinal timeline with a multilayer process that leaves little agreement on when the brain is mature [87]. As for intelligence, it seems that the more neurons in the brain, the more cognition one species has [88]. Furthermore, the hippocampus is one of the most important structures in the brain; it is associated with memory [49]. It is often linked with intelligence, even though it is much more complicated than we thought [89].

There were several limitations of this study. First, there is a lack of piglet brain references at same age for us to compare our findings on segmentation. Several published literatures that reported the pig brains of older age as listed in the segmentation method were carefully considered as our references to delineate the relative position of brain structures and to improve the precision of segmentation. Rather than fixating the brain with formalin for lack of supplements, we froze the brain in the -80°C freezer to keep it fresh. However, possible dehydration during sample handling—freezing, storage and dissolving—could lead to volume change of the brain structures.

The other limitation is the B_1 field inhomogeneity of the MR scanner, which can cause the changes of image contrast and lead to ambiguous boundaries of the brain structures.

4.5. SUMMARY

In this study, we analyzed the brain anatomy of neonatal piglets at the age of 12 days with ultrahigh-field 9.4T MR scanner and constructed a piglet brain database. The segmented brain structures provided references for future studies in *in vivo* assessment of brain growth and development of piglet brain.

5. *IN VIVO* AND *EX VIVO* PIGLET BRAIN COMPARISON

5.1. INTRODUCTION

Imaging is a valuable tool for studying the anatomy of the brain as we can obtain data on the brain's structures without doing dissection [90]. *In vivo* MRI can be exploited to track changes in the structure of interest without sacrificing the animal [81][91] allowing a timeline study to evaluate the changes in the anatomy [92]. However, *in vivo* MRI for animals can be affected by compromised image quality caused by breathing and other motions [93]. In addition, limited tolerance for anesthesia can restrict the time to acquire images with high qualities [92]. On the other hand, *ex vivo* MRI allows for longer scan time and tighter scanning sequences to acquire images with higher resolution and better contrast [81][92]. Additionally, a high dose of contrast agent can be managed to ameliorate the resolution and the contrast of images acquired *ex vivo* [92].

A few studies have been conducted to compare the difference between *in vivo* and *ex vivo* MR images. Some were done to compare images of mouse brain [90][92], and some were performed on human brain [93][94]. To date, there is insufficient research on the comparisons of *in vivo* and *ex vivo* MR images of piglet brain. In this study, two different low-resolution *in vivo* piglet brain MR images were acquired, along with high-resolution *ex vivo* MR images after the skulls were harvested. The volume of whole brain and five brain structures were measured and compared between the *in vivo* images using two different low-resolutions and the *ex vivo* images using high-resolution. We hypothesized that there would be no volume differences between the brain structures segmented from the *in vivo* and *ex vivo* images.

5.2. MATERIALS AND METHODS

5.2.1. Specimen preparation

A total of nineteen female piglets were obtained from the swineherd of the University of Illinois System. These piglets were raised under normal conditions through their age of 12 days. And all the procedures were performed following the guidelines of Care and Use of Laboratory Animals approved by the University of Illinois Institutional Animal Care and Use Committee (Approval number: 18-046).

The brains were harvested with skull for volume evaluations after those piglets were sacrificed. The dissected heads were rapid frozen in liquid nitrogen and stored in the -80 °C freezer to keep fresh. Each subject was moved from the -80 °C freezer to the -20 °C freezer before it was scheduled for scanning. The subject was thawed at 4 °C for 22 to 24 hours to allow the ice to dissolve and prepare the brain for scanning.

5.2.2. MRI acquisition

All MR images were performed with the 9.4T MR scanner (Agilent, Santa Clara, CA) at the age of 12 days.

The *in vivo* (low-resolution) MR images were performed using a two-dimensional fast spin-echo sequence with two sets of different scanning parameters with 150 mm ID birdcage volume RF coil (Rapid, Germany). Ten piglet brains were acquired with the first set of parameters: TR = 5000.00 ms, TE = 84.00 ms, ESP = 12 ms, segments/ESL = 32/8, $k_{zero} = 7$, average = 2, field of view = $140 \times 140 \text{ mm}^2$, data matrix = 256×256 , slices = 30, slice thickness = 2 mm, gap = 0.5 mm and voxel spacing— $0.5469 \times 0.5469 \times 2 \text{ mm}^3$. The total scanning time for each set of T₂-weighted image was 5 minutes and 30 seconds.

Nine piglet brains were acquired with the second set of parameters: TR = 5000.00 ms, TE = 84.00 ms, ESP = 12 ms, segments/ESL = 32/8, $k_{\text{zero}} = 7$, average = 2, field of view = 100×100 mm², data matrix = 256×256 , slices = 30, slice thickness = 2 mm, gap = 0.5 mm and voxel spacing— $0.3906 \times 0.3906 \times 2$ mm³. The total scanning time for each set of T₂-weighted image was 5 minutes and 30 seconds.

All the *ex vivo* (high-resolution) piglet brain images were acquired at resolution of $0.2344 \times 0.2539 \times 0.2539$ mm with the same MR scanner and the same parameters as described in Chapter 4.

5.2.3. Delineation and segmentation

To compare the *in vivo* and *ex vivo* images, five piglet brain structures—the cerebellum, the midbrain, the thalamus, the olfactory bulb, and the hippocampus—and the whole brain were delineated and segmented. All the structures and parts were performed manually using the ITK-SNAP software (Version 3.8.0). The references used to identify and locate the brain structures were the same as those in Chapter 4. Moreover, the piglet brain analyzed earlier were used as references to assist with segmenting the structures.

5.2.4. Analysis of structure volumes and statistics

Fourteen piglet brains were analyzed for comparison of *ex vivo* high-resolution and *in vivo* low-resolution images. Five sets of *in vivo* low-resolution images were blurred with artifacts and not clear enough to identify the regions of interest (ROIs). Pearson's correlation coefficients were calculated between measured volumes of each brain structure and of whole brain on *in vivo* low resolution and *ex vivo* high-resolution images. The Bland–Altman method was applied to evaluate

the volume difference and agreement between the two image sets [94][95]. The confidence intervals (CI) were determined as shown in Eq. (5-1):

$$CI = SE \times t \quad (5-1)$$

where SE is the standard error of the standard deviation, and t is the *t*-distribution value with n-1 degree of freedom (n is the number of sample). And the upper and lower limits of agreement (LOA) were calculated as shown in Eq. (5-2):

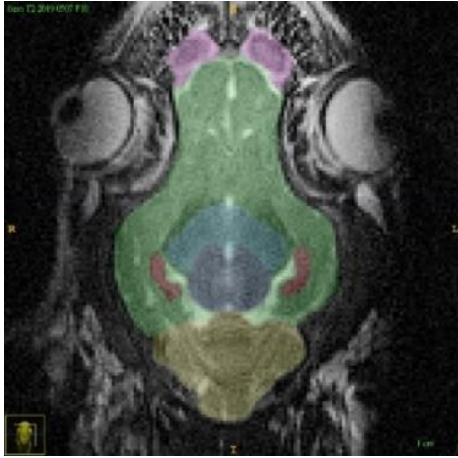
$$LOA = Mean \pm CI \quad (5-2)$$

Paired two-tailed *t*-tests were performed to compare the volumes of the *in vivo* and *ex vivo* images. A *p*-value less than .05 was considered statistically significant. All the statistical analyses and the plots were calculated and made using Excel (Microsoft Office 365, Microsoft, WA).

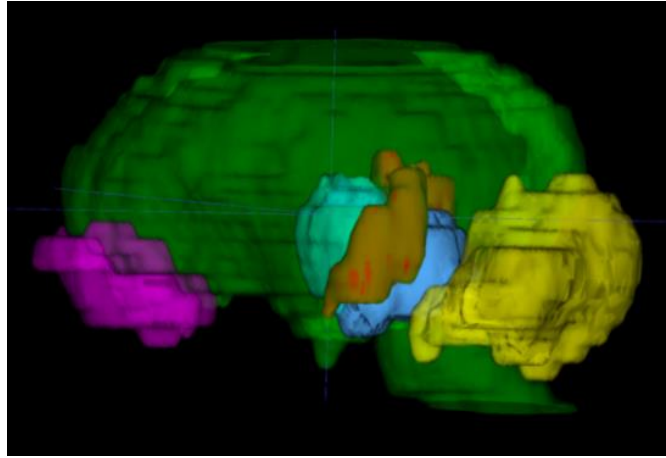
5.3. RESULTS

5.3.1. Piglet brain segmentation

High- and low-resolution images of 14 piglet brains were evaluated in this section. For both *in vivo* and *ex vivo* images, five brain structures were segmented manually: the hippocampus, the cerebellum, the thalamus, the midbrain, the olfactory bulb. The other parts of the brain were segmented along with the cerebral cortex (see Fig. 13 (A), (C)). Using the functions of the ITK-SNAP software, we reconstructed the brain with a 3D model, shown in Fig. 13 (B), (D). The red portion of the 3D model shows the hippocampus structure within the piglet brain. The yellow, the light blue, the grey-blue, and the pink portions represent the cerebellum, the thalamus, the midbrain, and the olfactory bulb, respectively. The green portion contains the cerebral cortex and the other structures of the piglet brain.



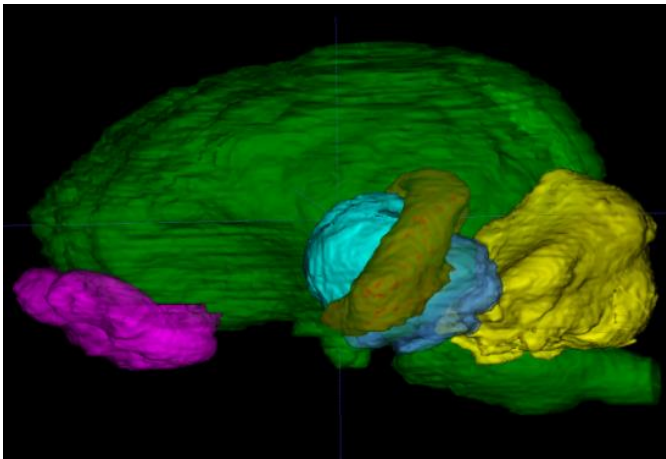
(A)



(B)



(C)



(D)

Figure 13. Reconstructions of high- and low-resolution T_2 -weighted piglet brain images with six structures: (A) The coronal view of in vivo piglet brain image. (B) Reconstructed model from in vivo piglet brain images. (C) The coronal view of ex vivo piglet brain. (D) Reconstructed model from ex vivo piglet brain images. The hippocampal region is labeled in red in this image; the cerebral cortex along with the other parts of the brain are labeled in green in this image; cerebellum which is in the lower part of the image is labeled in yellow; the thalamus is in the middle part of the brain near the hippocampus with the light blue label; the midbrain is the

structure that locates between the thalamus and the cerebellum is labeled with grey-blue, and the olfactory bulb that is in the upper part of the image is labeled with pink.

For the low-resolution images, two different image resolutions were acquired to be compared with the high-resolution images. Of the 14 piglet brains, images of eight were acquired with $0.5469 \times 0.5469 \times 2 \text{ mm}^3$ voxel size (R1), and images of the other six were acquired with $0.3906 \times 0.3906 \times 2 \text{ mm}^3$ voxel size (R2), as shown in Table IV. All the high-resolution images were acquired through a 3D FSE sequence with $0.2344 \times 0.2539 \times 0.2539 \text{ mm}^3$ voxel size.

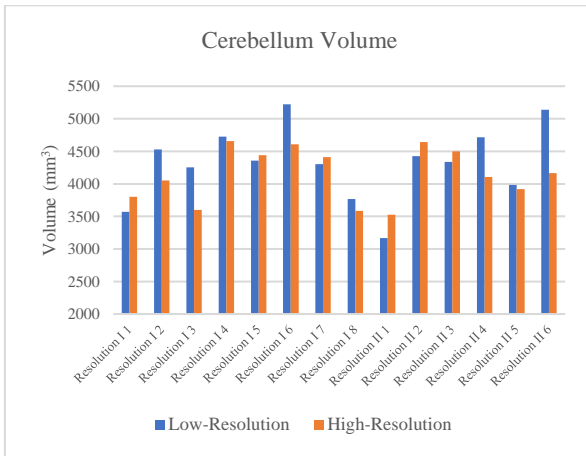
Table IV. Image resolution for fourteen low-resolution images

Resolution	Image Voxel Size (mm³)	Number
I	0.5469*0.5469*2	8
II	0.3906*0.3906*2	6
Total		14

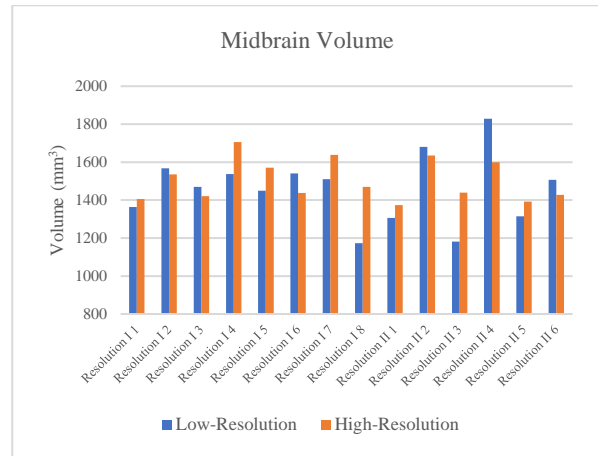
5.3.2. Analysis of the volumes of the structures

The volumes of structures of the high- and low-resolution images of the piglets are shown in Fig. 14. Eight of the 14 piglet brains had a higher cerebellum volume in the low-resolution image than in the high-resolution image. Image resolution I (R1) was used for five of them and the rest were from image resolution II (R2). Six of 14 piglet brains had a higher midbrain volume in the low-resolution images than in the high-resolution images. R1 and R2 contributed equally to those results. Eleven of 14 piglet brains had a higher thalamus volume in the low-resolution images than in the high-resolution images. R1 contributed to six of them and the rest were from R2. Only one olfactory bulb volume from the high-resolution image was higher compared to that from the low-resolution image, which belonged to the R1 image. Also, only two hippocampus volumes from the low-resolution images were higher than those from the high-resolution images, which all

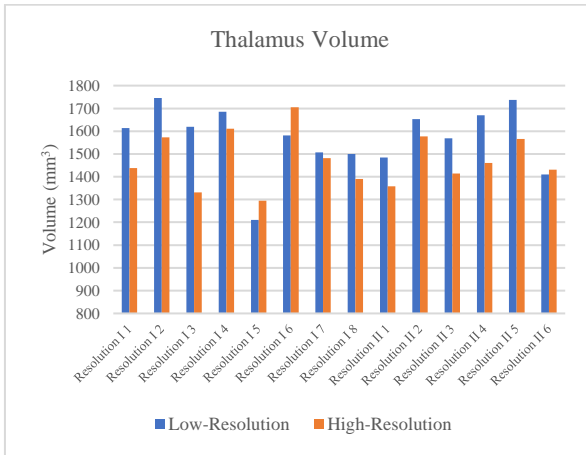
belonged to R1 images. At last, all the whole brain volumes from the high-resolution images were lower than those from the low-resolution images. These figures show that two-thirds of volumes of structures (such as the cerebellum, the thalamus, the olfactory bulb, and the whole brain) from low-resolution images tended to be overestimated compared to those from the high-resolution images.



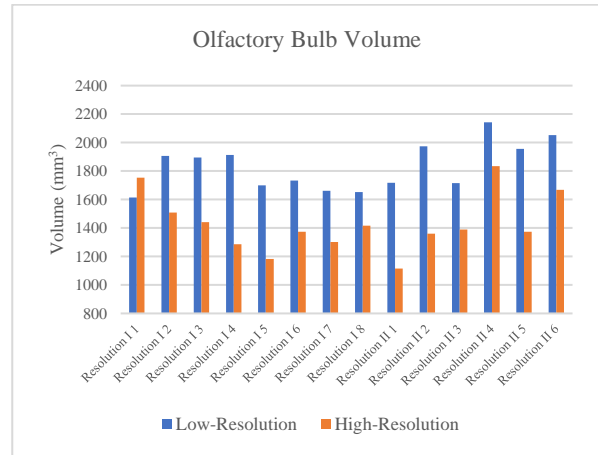
(A)



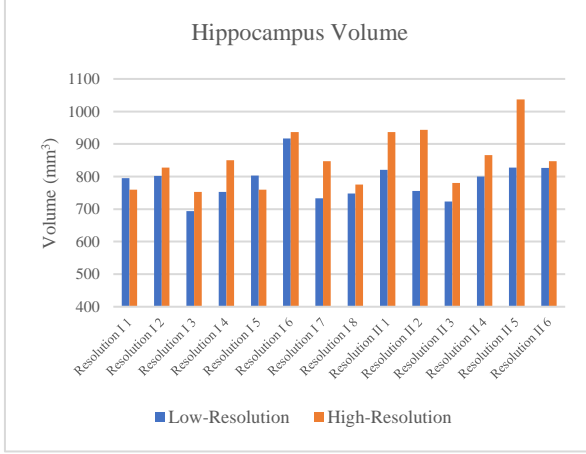
(B)



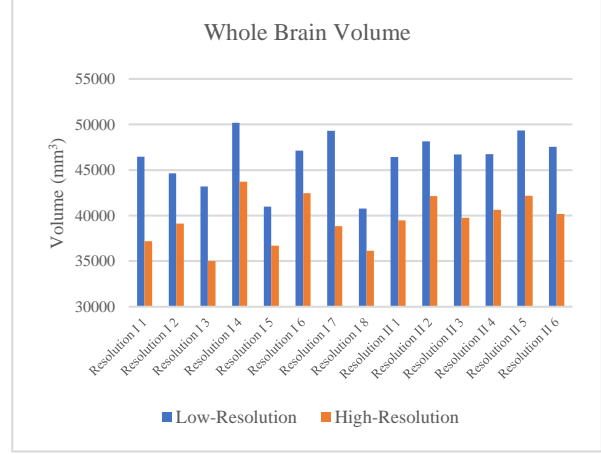
(C)



(D)



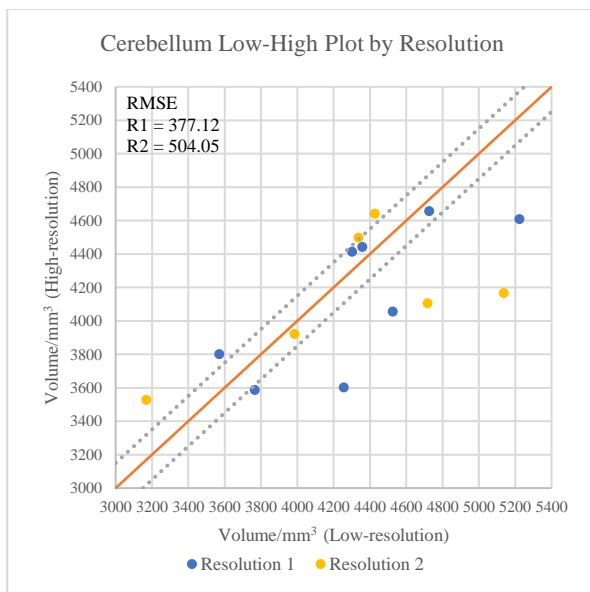
(E)



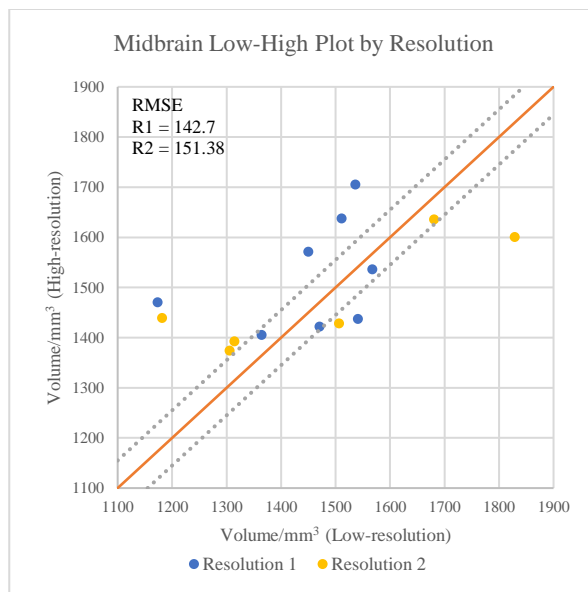
(F)

Figure 14. Volumes of structures from high- and low-resolution images at different image resolutions: (A) The cerebellum volume. (B) The midbrain volume. (C) The thalamus volume. (D) The olfactory bulb volume. (E) The hippocampus volume. (F) The whole-brain volume.

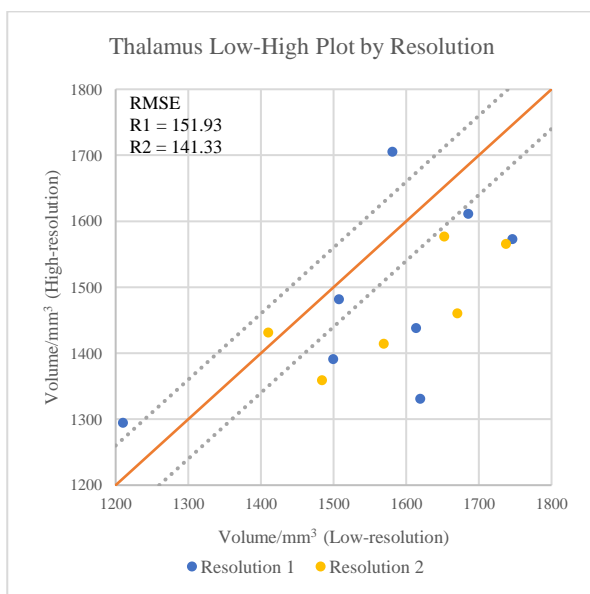
We plotted the volumes of the brain structures with both high- and low-resolution images, as seen in Fig. 15. The orange line in each image represents the ideal volumes at which the volumes of the structures from low-resolution images match the volumes from high-resolution images. Then, the two gray dotted lines represent the acceptable margins of error for each structure. The dots are scattered in each subfigure, and from the root mean square error (RMSE) indicates which image resolution is more precise for the volume of that structure. In other words, the dots show which low-resolution image is closer to the volume taken from the high-resolution image. The results showed that R1 tended to yield better results for the cerebellum, the midbrain, the olfactory bulb, and the hippocampus (Fig. 15 (A), (B), (D), (E)), while R2 tended to perform better for the thalamus and the whole brain (Fig. 15 (C), (F)).



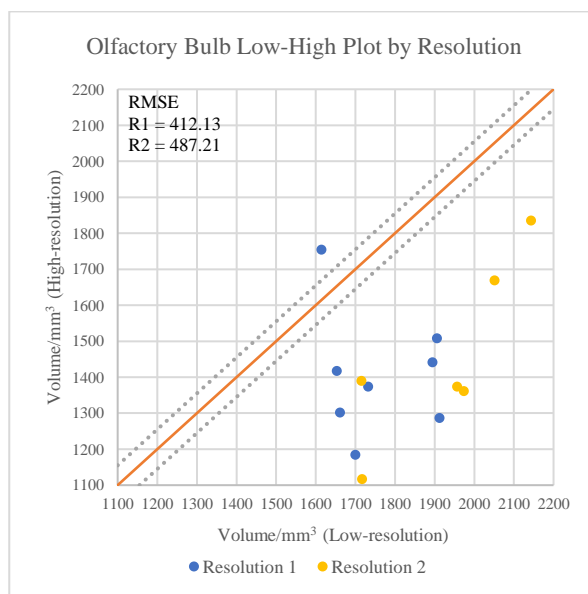
(A)



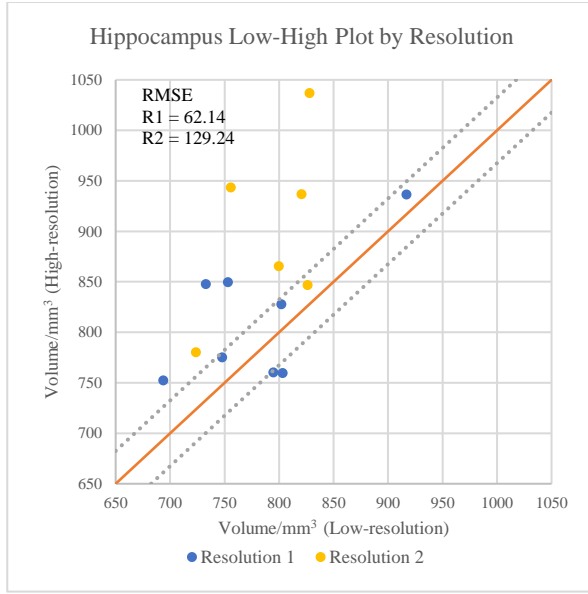
(B)



(C)



(D)



(E)

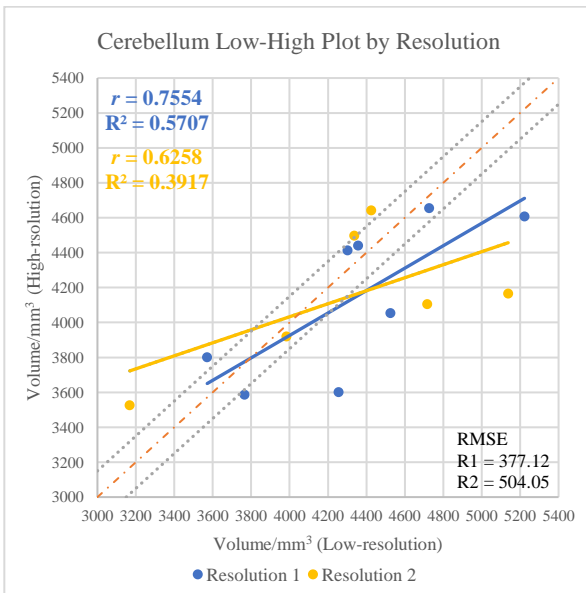


(F)

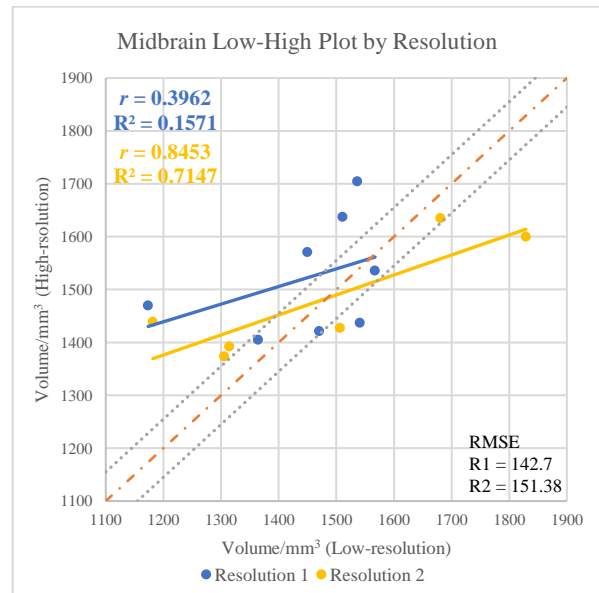
Figure 15. Plots of volumes of structures from high-resolution and low-resolution images with different image resolutions: (A) The cerebellum volume. (B) The midbrain volume. (C) The thalamus volume. (D) The olfactory bulb volume. (E) The hippocampus volume. (F) The whole-brain volume. Orange line is the ideal volume for the low-resolution images; Gray dotted lines are the acceptable margins of error for each structure; Blue dots represent R1; Yellow dots represent R2.

We conducted regression analysis for each resolution of the images of the six brain structures, as shown in Fig. 16. R1 yielded a better RMSE for most structures, but not all of them. The volumes of the cerebellum and the whole brain had Pearson correlation coefficient (r) and coefficients of determination (R^2) higher than 0.5. For R1 the r -values were 0.76 for both cerebellum and whole brain, while the R^2 values were 0.57 and 0.58 for the cerebellum and the whole brain, respectively (Fig. 16 (A), (F)). The volumes of the hippocampus from R1 had a Pearson's r of 0.63, but its R^2 was 0.4. This showed that there was some correlation between the high- and low-resolution images for the hippocampus, but it was not significant (Fig. 16 (E)). On

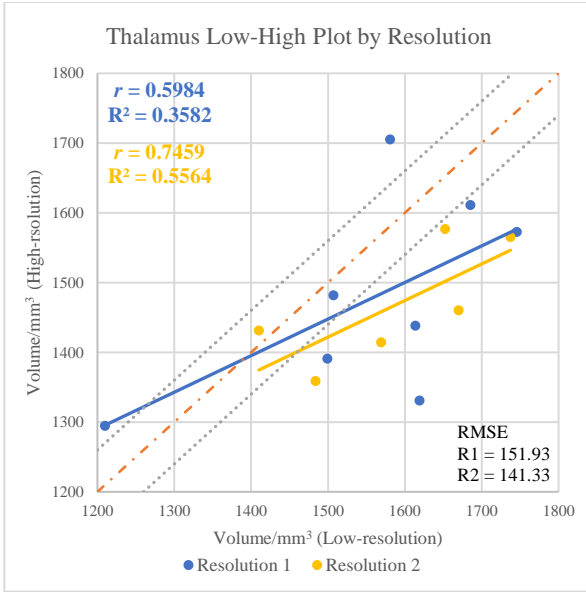
the other hand, not only did R2 yield better RMSE values for low- and high-resolution images for the thalamus and the whole brain, but it also had better results for the Pearson correlation analysis. For the thalamus, the r -value was 0.75 and the R^2 was 0.56—both above 0.5 (Fig 16 (C)). For the whole brain, R2 yielded an r -value of 0.88 and an R^2 value of 0.77 (Fig. 16 (F)). Neither the r -value nor the R^2 value was over 0.5 for the midbrain under R1, though its RMSE value was better than under R2. On the contrary, for the volume of the midbrain, the r -value was 0.85 and R^2 was 0.71 under R2 (Fig. 16 (B)). The Pearson correlation analysis of the volume of the olfactory bulb under R1 was not significant, while R2 showed a better result: the r -value was 0.84 and the R^2 was 0.7 (Fig. 16 (D)).



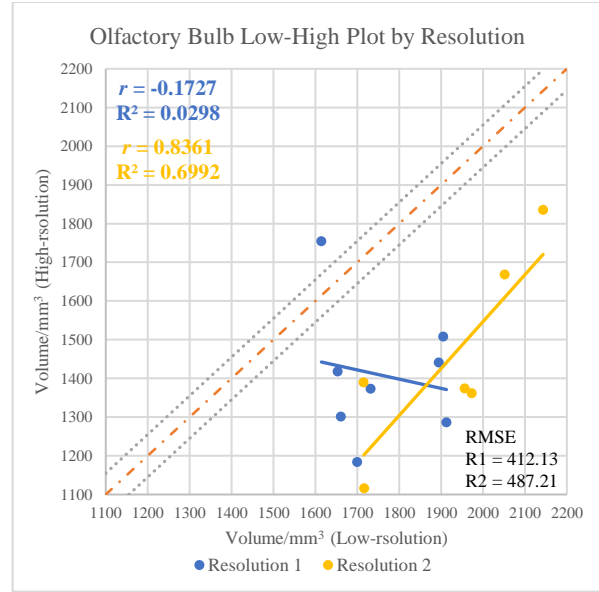
(A)



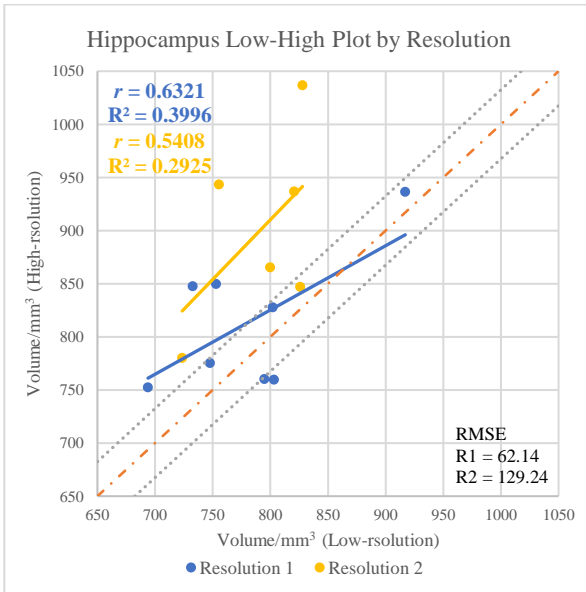
(B)



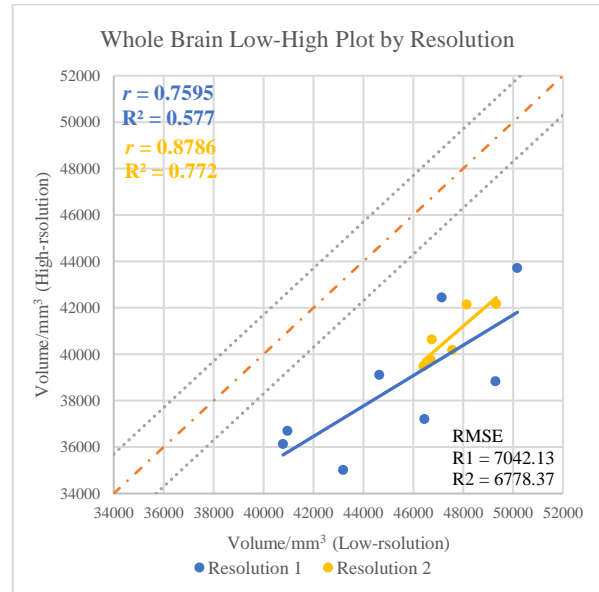
(C)



(D)



(E)

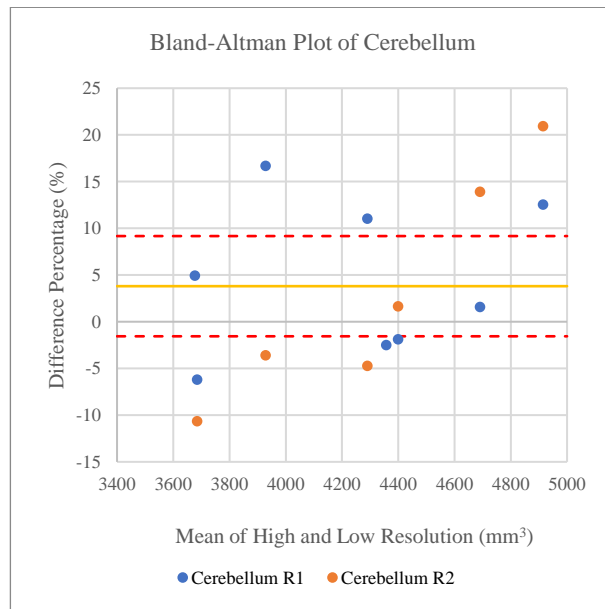


(F)

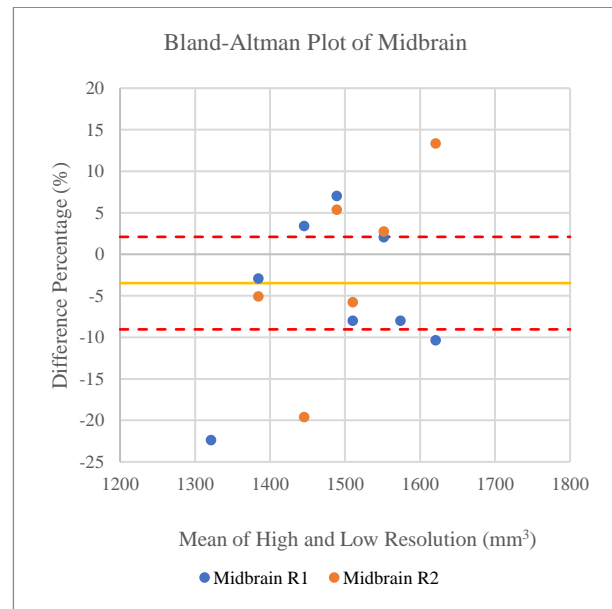
Figure 16. Plots of the volumes of brain structures at low-resolution and high-resolution with Pearson correlation analysis: (A) The cerebellum volume. (B) The midbrain volume. (C) The plot of thalamus volume. (D) The olfactory bulb volume. (E) The hippocampus volume. (F) The whole-brain volume.

We then conducted the Bland-Altman analysis to see if there was agreement between the *in vivo* and *ex vivo* images for five of the brain structures and the whole brain. The differences between high-resolution images and low-resolution images are shown in Fig. 17. The yellow line is the mean bias of the low-resolution *in vivo* images relative to the high-resolution *ex vivo* images. The two red dotted lines are the upper and lower limits of agreement (LOA). Generally, when the zero-difference line is within the range of the two LOA, it means there is agreement or a relationship between the two methods. Our results showed that there might be correlations between the high- and the low-resolution images of the cerebellum and the midbrain (Fig. 17 (A), (B)). The mean bias for the volume of the cerebellum was overestimated by 3.8% in the low-resolution images, while the mean bias was underestimated by -3.4% for the midbrain volume. At the same time, there were seven cerebellar volumes in the LOA range or within $\pm 5\%$, of which four were from the R1 images (Fig. 17 (A)). In addition, there were eight midbrain volumes in the LOA range or within $\pm 5\%$ and five of them were from R1 (Fig. 17 (B)). On the other hand, there was no agreement for the volumes of the thalamus, olfactory bulb, hippocampus, and the whole brain between *in vivo* and *ex vivo* images, and the bias for these structures was 6.24%, 25.1%, -7.78%, and 15.67%, respectively (Fig. 17 (C), (D), (E), (F)). There were 11 thalamus volumes overestimated by the low-resolution images, of which five results were from R2. Besides, two-sevenths of thalamus volume differences were within the acceptable value, which was no more than $\pm 5\%$. And half of them were from R1, the other were from R2 (Fig. 17 (C)). Only one volume for the olfactory bulb was underestimated by the low-resolution images, and it was from R1, the rest were overestimated. The percentage difference between the high- and low-resolution images for the olfactory bulb volume was huge; it ranged from -8.29% to 42.42%. Nevertheless, no subject had a difference in $\pm 5\%$ range (Fig. 17 (D)). For the differences in volume for the hippocampus,

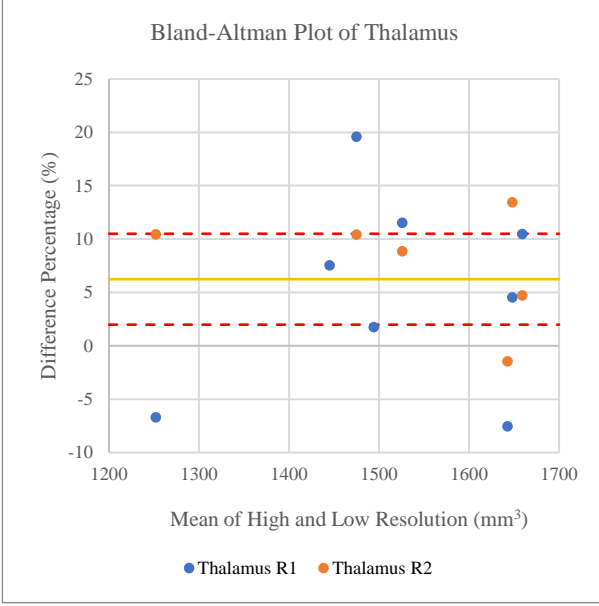
only two were overestimated, both of which were under R1. The range of volume difference for the hippocampus was from -22.4% to 5.62%, and five of the 14 volumes fell in the $\pm 5\%$ range (Fig. 17 (E)). All the whole brain volumes were overestimated by the low-resolution images, and all the volume differences were more than 10%. One subject from the R1 image even reached 23.76% (Fig. 17 (F)).



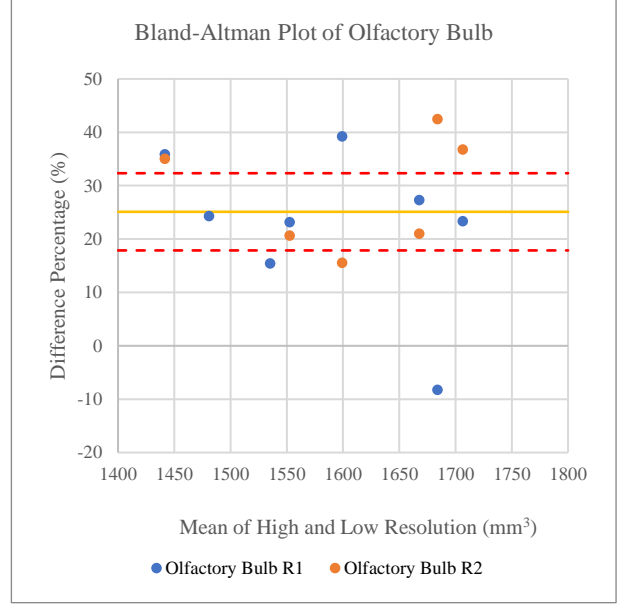
(A)



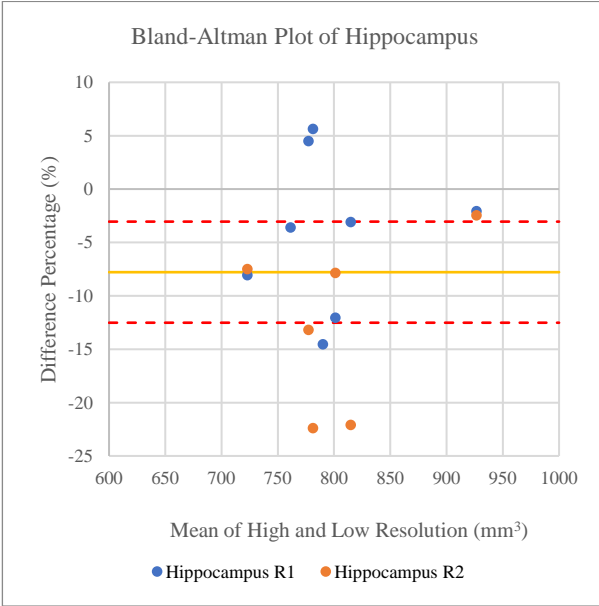
(B)



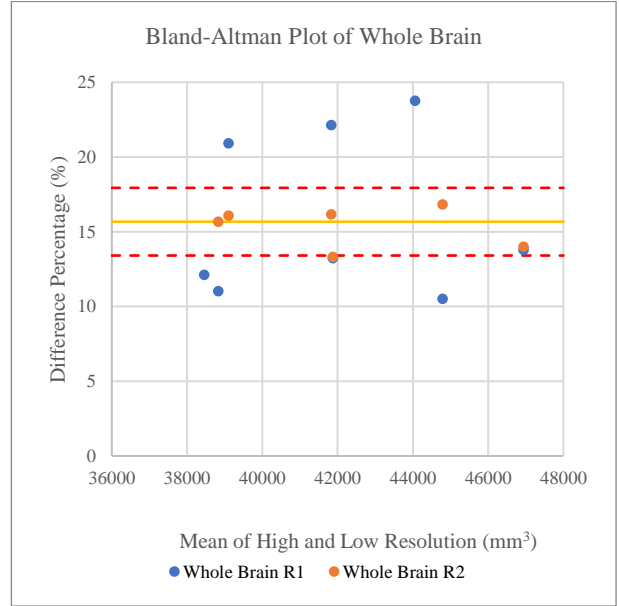
(C)



(D)



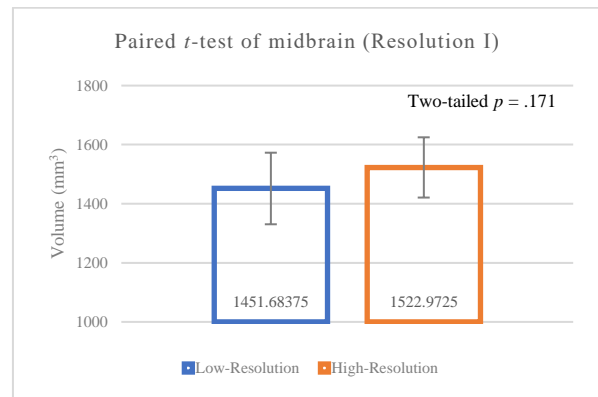
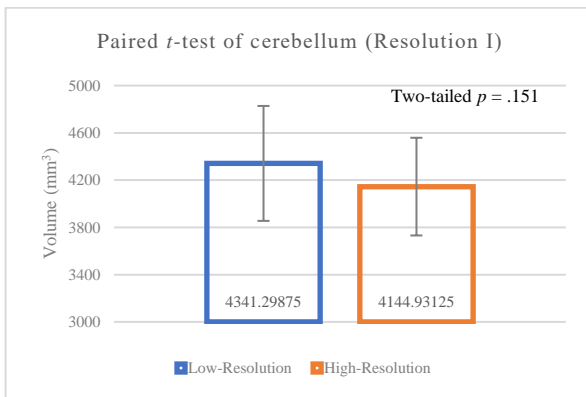
(E)



(F)

Figure 17. Bland-Altman plots of differences in volume from high-resolution and low-resolution images: (A) Cerebellum volume. (B) Midbrain volume. (C) Thalamus volume. (D) Olfactory bulb volume. (E) Hippocampus volume. (F) Whole-brain volume.

We conducted paired *t*-tests on the volumes of the structures from high- and R1 low-resolution images, and the results are shown in Fig. 18. For the cerebellum, the mean volumes from the *ex vivo* and the *in vivo* images were $4.145 \pm 0.414 \text{ cm}^3$ and $4.341 \pm 0.486 \text{ cm}^3$, respectively. The *p*-value was .15 in the two-tailed *t*-test, which showed that there was no significant difference for the cerebellum volumes from the two images (Fig. 18 (A)). For the midbrain, the mean volume from the high-resolution image was $1.523 \pm 0.102 \text{ cm}^3$ and the mean from the low-resolution image was $1.452 \pm 0.121 \text{ cm}^3$. In the case, the *p*-value for the test was .17, which also showed no significant difference (Fig. 18 (B)). For the thalamus, the means of the volumes were $1.478 \pm 0.134 \text{ cm}^3$ and $1.558 \pm 0.153 \text{ cm}^3$, respectively, with a *p*-value of .15 for the paired *t*-test (Fig. 17 (C)). For the hippocampus, means volumes were $0.814 \pm 0.060 \text{ cm}^3$ and $0.781 \pm 0.063 \text{ cm}^3$, and there was no significant difference between the segmented volumes from two image resolutions for the paired *t*-test since the *p*-value was .14 (Fig. 18 (E)). For the olfactory bulb, means volumes were $1.408 \pm 0.161 \text{ cm}^3$ and $1.759 \pm 0.117 \text{ cm}^3$, with a *p*-value of .0035 for the paired *t*-test. This showed that there was significant difference from the images made with the two resolutions (Fig. 18 (D)). For the whole brain, the means volumes were $38.642 \pm 2.866 \text{ cm}^3$ and $45.335 \pm 3.326 \text{ cm}^3$, and there was a significant difference between the volumes from two resolutions for the paired *t*-test since the *p*-value was 8.51×10^{-5} (Fig. 18 (F)).



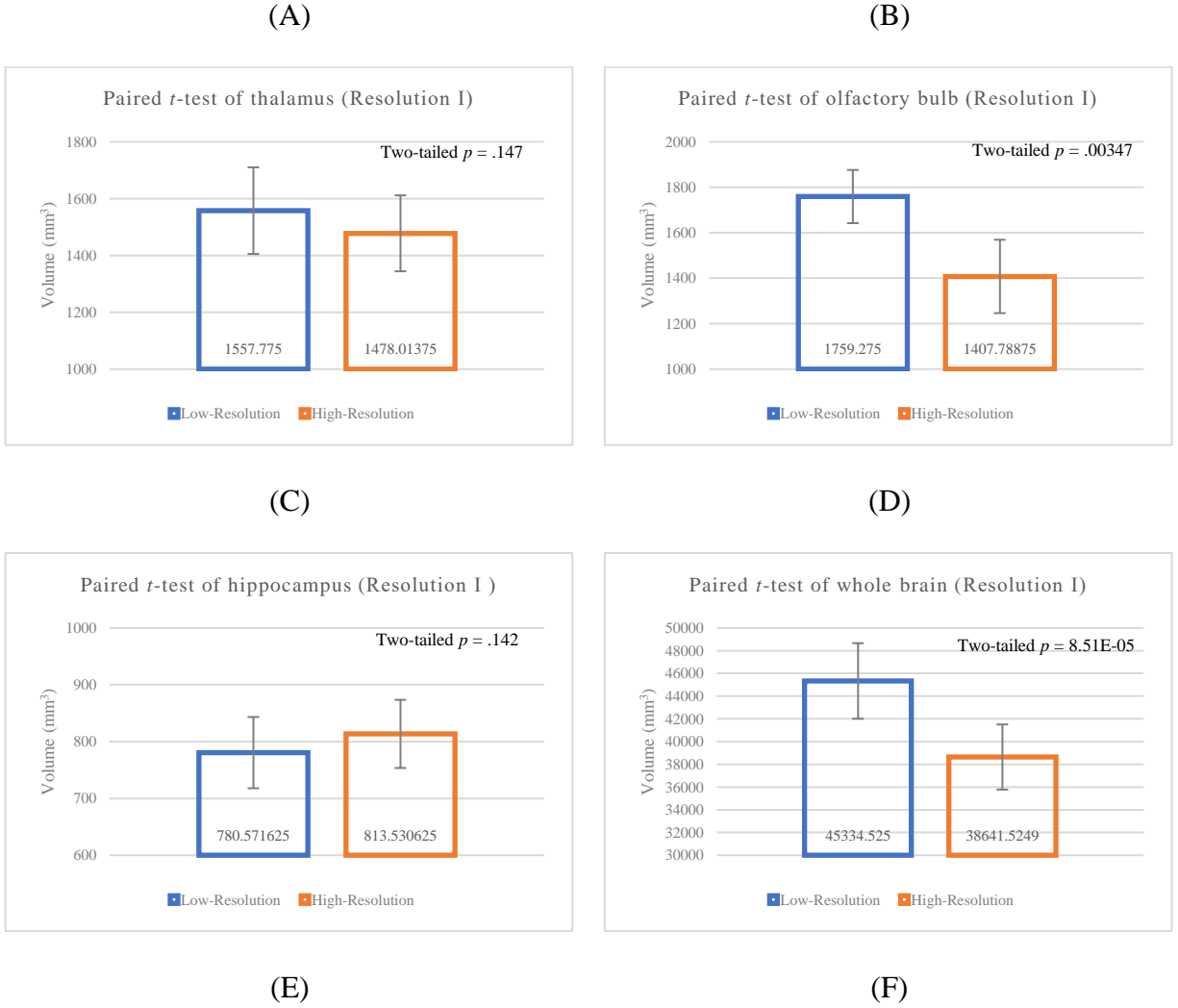
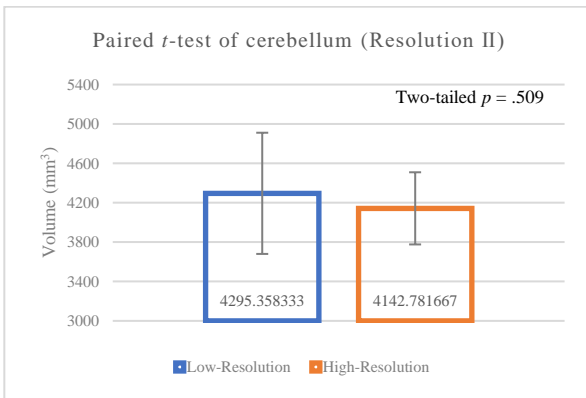


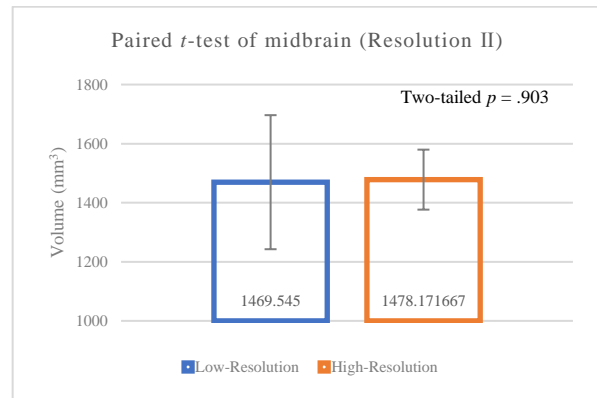
Figure 18. Result of paired *t*-tests to compare the volumes from high- and low-resolution images for six brain structures, using resolution R1. (A) The cerebellum volume. (B) The midbrain volume. (C) The thalamus volume. (D) The olfactory bulb volume. (E) The hippocampus volume. (F) The total volume of the brain.

We also conducted paired *t*-tests on the volumes of the structures from the high- and R2 low-resolution images, and the results are shown in Fig. 19. The mean volumes from the R2 low-resolution images for the cerebellum, the midbrain, the thalamus, the olfactory bulb, the hippocampus and the whole brain were $4.295 \pm 0.616 \text{ cm}^3$, $1.470 \pm 0.227 \text{ cm}^3$, $1.587 \pm 0.113 \text{ cm}^3$,

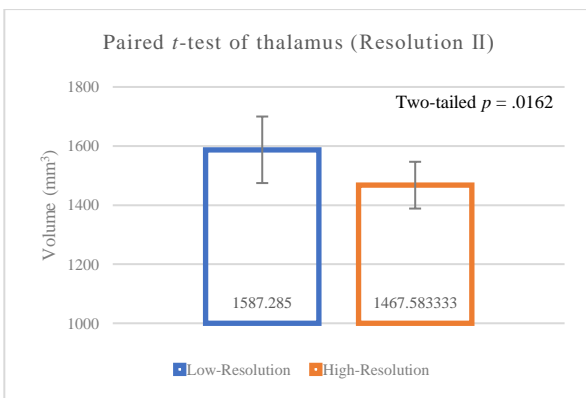
$1.926 \pm 0.160 \text{ cm}^3$, $0.792 \pm 0.039 \text{ cm}^3$ and $47.486 \pm 1.010 \text{ cm}^3$, respectively. And those volumes from high-resolution images were $4.143 \pm 0.366 \text{ cm}^3$, $1.478 \pm 0.102 \text{ cm}^3$, $1.468 \pm 0.079 \text{ cm}^3$, $1.457 \pm 0.233 \text{ cm}^3$, $0.901 \pm 0.082 \text{ cm}^3$ and $40.727 \pm 1.069 \text{ cm}^3$, respectively. The p -values of the paired t -tests showed that there was no significant difference between the R2 low-resolution images and the high-resolution images for the cerebellum and the midbrain, which had p -values of .51 and .9, respectively (Fig 19 (A), (B)). On the other hand, there were significant differences between the volumes from the two image resolutions for the thalamus, the olfactory bulb, the hippocampus and the whole brain. Their p -values were .016, 5.09×10^{-4} , .017, and 8.65×10^{-7} , respectively.



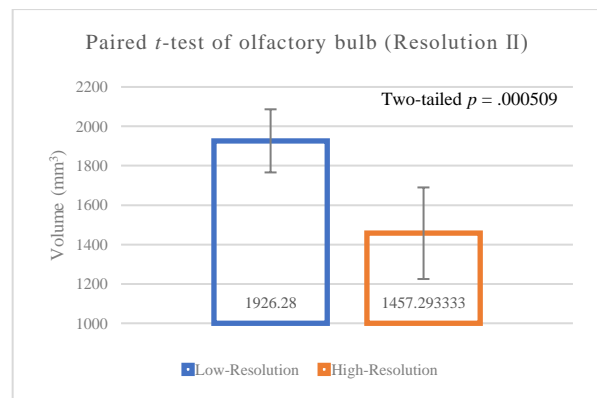
(A)



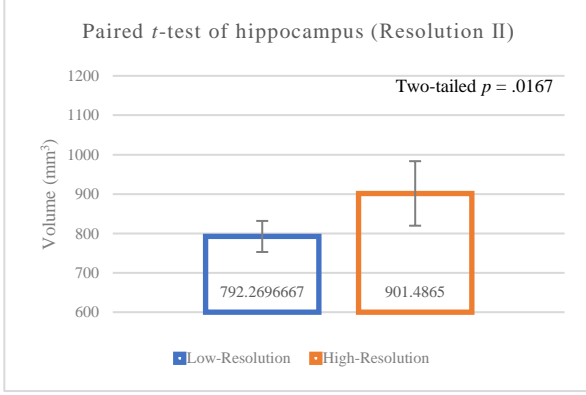
(B)



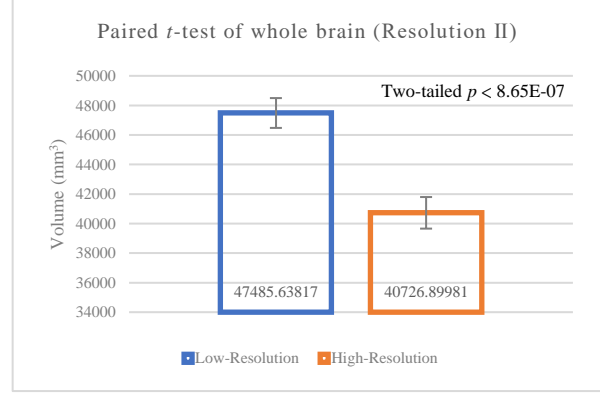
(C)



(D)



(E)



(F)

Figure 19. Result of paired *t*-tests to compare the volumes from high- and low-resolution images for six brain structures, using resolution R2. (A) The cerebellum volume. (B) The midbrain volume. (C) The thalamus volume. (D) The olfactory bulb volume. (E) The hippocampus volume. (F) The total volume of the brain.

5.4. DISCUSSION

This is the first comparison of *in vivo* and *ex vivo* MR images performed on 12-day-old neonatal piglet brain with 9.4T ultrahigh magnetic field. We found the measured volumes of cerebellum and midbrain *in vivo* had no difference to those measured *ex vivo*. The volumes of hippocampus measured *in vivo* with $0.5469 \times 0.5469 \times 2 \text{ mm}^3$ image voxel size were similar to their *ex vivo* measurements. The volumes of olfactory bulb, thalamus and whole brain volume showed significant difference between *in vivo* and *ex vivo* measurements.

Six brain structures—the cerebellum, the midbrain, the thalamus, the olfactory bulb, the hippocampus and the total brain—from 14 piglet brains were compared between the volumes measured from *ex vivo* high-resolution images and those from two *in vivo* low-resolution results. As we evaluated each structure from the 14 piglets individually, we found that the inaccuracy of estimating the volumes of the structures could come from both R1 and R2 images. The voxel size

for the R1 low-resolution image was about 0.598 mm^3 , and that for the R2 low-resolution image was about 0.305 mm^3 . The voxel size for the high-resolution image was about 0.015 mm^3 . The high-resolution images should have more accurate measurements than low-resolution images. However, when comparing to *ex vivo* high-resolution images, for each structure, *in vivo* images either underestimated or overestimated the volume when compared to their *ex vivo* images. Combining the results of RMSE and the paired *t*-test, we found that the results from resolution R1 were better than those from resolution R2 for the cerebellum, the midbrain and the hippocampus. They had lower RMSE values and showed no volume difference between the *in vivo* and *ex vivo* images. On the other hand, resolution R2 might be a better resolution for estimating the whole brain volume. Even though the paired *t*-tests showed there was a difference between the high- and low-resolution images, the R^2 value (0.77) was the highest for all the structures measured. For the cerebellum, the second largest structure in the brain, six out of fourteen estimation of the volumes from *in vivo* images tended to be underestimated, while both R1 and R2 identified three subjects that had volume difference within $\pm 5\%$. Moreover, the cerebellum of one subject from R1 had a percentage difference of nearly 5%, as shown in Fig. 17(A), while there were five results for the midbrain that were within the $\pm 5\%$ range. Three were from R1, and two were from R2. But the most inaccurate estimation was from R1 as well (-22.42%) (Fig. 17(B)). On the other hand, most of the volumes of the thalamus and the olfactory bulb were overestimated. Only four thalamus volumes and one olfactory bulb volume were within the range of reasonable error (Fig. 17(C), (D)). Because there was no correlation between the RMSE and the paired *t*-test for the two structures, there was less discussion on both structures. As for the hippocampus, the volumes of 12 subjects were underestimated. Although most of the hippocampal volumes obtained from the low-resolution images were underestimated, five of them had errors within $\pm 5\%$ range, and four of

them were from R1 images (Fig. 17 (E)). All the whole-brain volumes were overestimated, and the errors were more than 10%, but the volume difference from R2 images tended to be less (Fig. 17 (F)).

The partial volume effect could be one of the factors that caused a difference between *in vivo* and *ex vivo* images. In addition, the inhomogeneity of the B₁ field could affect the image quality that led to ambiguous boundaries of the structures. Tissue variation after the skulls were harvested also could be a reason for this as the piglet brains were not fixed before *ex vivo* imaging. The acquisition time for each high-resolution *ex vivo* image was about 102 minutes in this study. However, it only took 5 minutes and 30 seconds to acquire each low-resolution *in vivo* image. Therefore, when a low-resolution image is clear enough and when the segmented structure is in the proper size and shape (like the midbrain), it might be more efficient to take low-resolution images than high-resolution images.

There were some limitations to this study. For one thing, there was not enough time for us to acquire *in vivo* brain images since there is limited tolerance for a neonatal piglet at the age of 12 days under anesthesia. In addition, besides scanning each piglet brain, the whole body of each piglet was scheduled to be scanned during one period of anesthesia. The motion artifact caused by respiration and the heartbeat could not be avoided, which led to ambiguous boundaries of structures. Another limitation was the lack of a brain atlas for a piglet at this age, which resulted in uncertainty in defining boundaries of structures.

5.5. SUMMARY

Our results from *in vivo* and *ex vivo* MR images comparison can provide guidance for proper handling brain samples for further imaging related studies and can serve as a reference for

refining the protocol for acquiring *in vivo* images. Further studies to build a standard neonatal piglet brain atlas and the piglet brain database according to early stages of brain development will benefit brain development and neurological studies using piglet as a translational animal model.

6. CONCLUSION

6.1. SUMMARY

The pig brain is an ideal animal model to be an alternative subject to the human brain. In our study, we investigated the anatomical brain structure of neonatal piglets at the age of 12 days. On average, the cerebral cortex, the cerebellum, and the brain stem were the top three structures in the piglet brain. Besides, the thalamus, which was the major structure of the diencephalon, and the olfactory bulb constituted 3.73% and 3.55% of the total brain, respectively. Furthermore, the structure related to memory and cognition, the hippocampus, represented 2.13% of the piglet brain. The corpus callosum, which serves as the bridge between the left and the right cerebral cortex, contributed only 0.43% at this age. Also, we tested the fitness of the volumes of structures between the *in vivo* MR images and *ex vivo* MR images. Because of several advantages of *ex vivo* MRI, we set it as the standard in our comparison. The results showed that our *in vivo* MRI and *ex vivo* MRI did not align well with each other. However, among six evaluated structures, the cerebellum, the midbrain and the hippocampus showed better results when their images were acquired with the R1 resolution ($0.5469 \times 0.5469 \times 2 \text{ mm}^3$), while the whole brain showed better results when its image was acquired with R2 resolution ($0.3906 \times 0.3906 \times 2 \text{ mm}^3$). Our results provided a reference of the neonatal piglet brain and set a reference for *in vivo* piglet brain MRI.

6.2. FUTURE WORK

This study provides a glance at the anatomy of the neonatal piglet brain, but it is merely an initial work. Not only do we need to increase the sample size to enlarge the database, but we must also build a standard piglet brain atlas that includes much more detail about the sub-tissue of the piglet brain, as the mouse brain atlas does. In addition, our *in vivo* scanning protocols must be refined to improve the accuracy of *in vivo* segmentation. In this way, advantages of the *in vivo* image can be preserved when acquiring the image, while the results align well with the *ex vivo* result.

7. REFERENCES

- [1] R. G. M. Morris *et al.*, “Consensus Statement on European Brain Research: the need to expand brain research in Europe – 2015,” *Eur. J. Neurosci.*, vol. 44, no. 3, pp. 1919–1926, 2016, doi: 10.1111/ejn.13236.
- [2] D. S. Bassett and O. Sporns, “Network Neuroscience,” *Nat. Neurosci.*, vol. 20, no. 3, pp. 353–364, 2017, doi: 10.2307/j.ctt9qh0x7.12.
- [3] B. Alexander *et al.*, “A new neonatal cortical and subcortical brain atlas: the Melbourne Children’s Regional Infant Brain (M-CRIB) atlas,” *Neuroimage*, vol. 147, pp. 841–851, 2017, doi: 10.1016/j.neuroimage.2016.09.068.
- [4] L. Gui, R. Lisowski, T. Faundez, P. S. Hüppi, F. Lazeyras, and M. Kocher, “Morphology-driven automatic segmentation of MR images of the neonatal brain,” *Med. Image Anal.*, vol. 16, no. 8, pp. 1565–1579, 2012, doi: 10.1016/j.media.2012.07.006.
- [5] M. S. Conrad, R. N. Dilger, and R. W. Johnson, “Brain growth of the domestic pig (*Sus scrofa*) from 2 to 24 weeks of age: A longitudinal MRI study,” *Dev Neurosci.*, vol. 34, no. 4, pp. 291–298, 2012, doi: 10.1038/jid.2014.371.
- [6] N. M. Lind, A. Moustgaard, J. Jelsing, G. Vajta, P. Cumming, and A. K. Hansen, “The use of pigs in neuroscience: Modeling brain disorders,” *Neurosci. Biobehav. Rev.*, vol. 31, no. 5, pp. 728–751, 2007, doi: 10.1016/j.neubiorev.2007.02.003.
- [7] H. Watanabe, F. Andersen, C. Z. Simonsen, S. M. Evans, A. Gjedde, and P. Cumming, “MR-based statistical atlas of the Göttingen minipig brain,” *NeuroImage*, vol. 14, no. 5, pp. 1089–1096, 2001, doi: 10.1006/nimg.2001.0910.

- [8] C. Fabris, B. Cozzi, A. Hay-Schmidt, B. Naver, and M. Møller, “Demonstration of an Orexinergic Central Innervation of the Pineal Gland of the Pig,” *J. Comp. Neurol.*, vol. 471, no. 2, pp. 113–127, 2004, doi: 10.1002/cne.20007.
- [9] G. L. Manno, D. Gyllborg, S. Codeluppi, K. Nishimura, C. Salto, A. Zeisel, L. E. Borm, S. R.W. Stott, E. M. Toledo, J. C. Villaescusa, Peter Lönnnerberg, J. Ryge, R. A. Barker, E. Arenas, and S. Linnarsson, “Molecular Diversity of Midbrain Development in Resource Molecular Diversity of Midbrain Development in Mouse , Human , and Stem Cells,” *Cell*, vol. 167, no. 2, pp. 566–580, 2016, doi: 10.1016/j.cell.2016.09.027.
- [10] B. Nitsche *et al.*, “A stereotaxic breed-averaged, symmetric T2w canine brain atlas including detailed morphological and volumetrical data sets,” *Neuroimage*, vol. 187, no. September 2017, pp. 93–103, 2019, doi: 10.1016/j.neuroimage.2018.01.066.
- [11] P. Brambilla, A. Hardan, S. U. D. Nemi, J. Perez, J. C. Soares, and F. Barale, “Brain anatomy and development in autism : review of structural MRI studies,” *Brain Res. Bull.*, vol. 61, pp. 557–569, 2003, doi: 10.1016/j.brainresbull.2003.06.001.
- [12] W. D. Foltz and D. A. Jaffray, “Principles of Magnetic Resonance Imaging,” *Radiat. Res.*, vol. 177, no. 4, pp. 331–348, 2012, doi: 10.1667/RR2620.1.
- [13] P. C. Lauterbur, “Image formation by induced local interactions examples employing nuclear magnetic resonance,” *Nature*, vol. 242, pp. 190–191, 1973.
- [14] J. C. McGowan, “Basic Principles of Magnetic Resonance Imaging,” *Neuroimaging Clin. N. Am.*, vol. 18, no. 4, pp. 623–636, 2008, doi: 10.1016/j.nic.2008.06.004.
- [15] N. B. Smith and A. Webb, *Introduction to Medical Imaging Physics, Engineering and*

Clinical Applications. 2011.

- [16] I. E. Holm, A. K. O. Alstrup, and Y. Luo, “Genetically modified pig models for neurodegenerative disorders,” *J. Pathol.*, vol. 238, no. 2, pp. 267–287, 2016, doi: 10.1002/path.4654.
- [17] R. H. Hashemi, C. J. Lisanti, and W. G. Bradley, Jr., “2 Basic principles of MRI,” in *MRI The Basic*, 3rd Editio., 2010, pp. 16–30.
- [18] R. J. M. Van Geuns *et al.*, “Basic principles of magnetic resonance imaging,” *Prog. Cardiovasc. Dis.*, vol. 42, no. 2, pp. 149–156, 1999, doi: 10.1016/S0033-0620(99)70014-9.
- [19] B. M. Dale, M. A. Brown, and R. C. Semelka, “CHAPTER 1 Production of net magnetization,” in *MRI Basic Principles and Applications*, 5th Editio., 2015, pp. 1–9.
- [20] V. P. B. Grover, J. M. Tognarelli, M. M. E. Crossey, I. J. Cox, S. D. Taylor-Robinson, and M. J. W. McPhail, “Magnetic Resonance Imaging: Principles and Techniques: Lessons for Clinicians,” *J. Clin. Exp. Hepatol.*, vol. 5, no. 3, pp. 246–255, 2015, doi: 10.1016/j.jceh.2015.08.001.
- [21] R. H. Hashemi, C. J. Lisanti, and W. G. Bradley, Jr., “3 Radio Frequency Pluse,” in *MRI The Basic*, 3rd Editio., 2010, pp. 32–39.
- [22] R. H. Hashemi, C. J. Lisanti, and W. G. Bradley, Jr., “4 T1, T2, and T2*,” in *MRI The Basic*, 3rd Editio., 2010, pp. 40–47.
- [23] B. M. Dale, M. A. Brown, and R. C. Semelka, “CHAPTER 3 Relaxation,” in *MRI Basic Principles and Applications*, 5th Editio., 2015, pp. 17–25.
- [24] R. H. Hashemi, C. J. Lisanti, and W. G. Bradley, Jr., “5 TR, TE, and Tissue Contrast,” in

- MRI The Basic*, 3rd Editio., 2010, pp. 48–56.
- [25] R. H. Hashemi, C. J. Lisanti, and W. G. Bradley, Jr., “8 Pulse Sequences Part II (Spin Echo),” in *MRI The Basic*, 3rd Editio., 2010, pp. 83–89.
 - [26] B. M. Dale, M. A. Brown, and R. C. Semelka, “CHAPTER 2 Concepts of magnetic resonance,” in *MRI Basic Principles and Applications*, 5th Editio., 2015, pp. 10–16.
 - [27] R. H. Hashemi, C. J. Lisanti, and W. G. Bradley, Jr., “6 Tissue Contrast : Some Clinical Applications,” in *MRI The Basic*, 3rd Editio., 2010, pp. 57–73.
 - [28] R. H. Hashemi, C. J. Lisanti, and W. G. Bradley, Jr., “10 Image Construction : Part I (Slice Selection),” in *MRI The Basic*, 3 rd Editi., 2010, pp. 98–107.
 - [29] B. M. Dale, M. A. Brown, and R. C. Semelka, “CHAPTER 4 Principles of magnetic resonance imaging-1,” in *MRI Basic Principles and Applications*, 5th Editio., 2015, pp. 26–38.
 - [30] R. H. Hashemi, C. J. Lisanti, and W. G. Bradley, Jr., “11 Image Construction : Part II (Spatial Encoding),” in *MRI The Basic*, 3rd Editio., 2010, pp. 108–122.
 - [31] R. H. Hashemi, C. J. Lisanti, and W. G. Bradley, Jr., “9 Fourier Transform,” in *MRI The Basic*, 4th Editio., 2018, pp. 96–101.
 - [32] B. M. Dale, M. A. Brown, and R. C. Semelka, “CHAPTER 5 Principles of magnetic resonance imaging-2,” in *MRI Basic Principles and Applications*, 5th Editio., 2015, pp. 39–64.
 - [33] R. H. Hashemi, C. J. Lisanti, and W. G. Bradley, Jr., “19 Fast Spin Echo,” in *MRI The Basic*, 3rd Editio., 2010, pp. 217–232.

- [34] R. H. Hashemi, C. J. Lisanti, and W. G. Bradley, Jr., “20 Gradient Echo: Part I (Basic Principles),” in *MRI The Basic*, 3rd Editio., 2010, pp. 233–246.
- [35] N. M. Gage and B. J. Baars, “The Brain,” in *Fundamentals of Cognitive Neuroscience: A Beginner’s Guide (Second Edition)*, 2018, pp. 17–52.
- [36] C. Watson, M. Kirkcaldie, and G. Paxinos, “Chapter 3 A map of the brain,” in *The Brain: An Introduction to Functional Neuroanatomy*, 2010, pp. 25–42.
- [37] C. Watson, M. Kirkcaldie, and G. Paxinos, “Chapter 2 Central nervous system basics—the brain and spinal cord,” in *The Brain: An Introduction to Functional Neuroanatomy*, 2010, pp. 11–24.
- [38] D. Pandya, B. Seltzer, M. Petrides, and P. B. Cipolloni, “Part I History of Architecture, Connections, and Dual Origin of Cerebral Cortex,” in *Cerebral Cortex : Architecture, Connections, and the Dual Origin Concept*, 2015, pp. 1–58.
- [39] V. Fernández, C. Llinares-Benadero, and V. Borrell, “Cerebral cortex expansion and folding : what have we learned ?,” *EMBO*, vol. 35, no. 10, pp. 1021–1044, 2016.
- [40] A. Schaefer *et al.*, “Local-Global Parcellation of the Human Cerebral Cortex from Intrinsic Functional Connectivity MRI,” *Cereb. Cortex*, vol. 28, no. 9, pp. 3095–3114, 2018, doi: 10.1093/cercor/bhx179.
- [41] T. Butts, M. J. Green, and R. J. T. Wingate, “Development of the cerebellum : simple steps to make a ‘ little brain ,’” *Development*, vol. 141, pp. 4031–4041, 2014, doi: 10.1242/dev.106559.
- [42] C. Limperopoulos, “The vulnerable immature cerebellum,” *Semin. Fetal Neonatal Med.*,

- vol. 21, no. 5, pp. 293–294, 2016, doi: 10.1016/j.siny.2016.07.002.
- [43] M. F. Roussel and M. E. Hatten, “Cerebellum: Development and Medulloblastoma,” *Curr. Top. Dev. Biol.*, vol. 94, pp. 235–282, 2011, doi: 10.1016/B978-0-12-380916-2.00008-5.Cerebellum.
- [44] L. Donnelly, “The brain : functional divisions,” *Physiology*, vol. 21, no. 6, pp. 322–327, 2020, doi: 10.1016/j.mpaic.2020.03.004.
- [45] Y. Wu, C. Stoodley, M. Brossard-Racine, K. Kapse, G. Vezina, J. Murnick, A. J. du Plessis, and C. Limperopoulos, “Altered local cerebellar and brainstem development in preterm infants,” *Neuroimage*, vol. 213, no. 116702, 2020, doi: 10.1016/j.neuroimage.2020.116702.
- [46] C. H. Gibbons, *Basics of autonomic nervous system function*, 1st ed., vol. 160. Elsevier B.V., 2019.
- [47] A. Minagar *et al.*, “The thalamus and multiple sclerosis,” *Neurology*, vol. 80, pp. 210–219, 2013, [Online]. Available: <https://www.ncbi.nlm.nih.gov/pmc/articles/PMC3589190/pdf/WNL204561.pdf>.
- [48] K. Mori, H. Manabe, K. Narikiyo, and N. Onisawa, “Olfactory consciousness and gamma oscillation couplings across the olfactory bulb, olfactory cortex, and orbitofrontal cortex,” *Front. Psychol.*, vol. 4, no. OCT, pp. 1–13, 2013, doi: 10.3389/fpsyg.2013.00743.
- [49] K. S. Anand and V. Dhikav, “Hippocampus in health and disease: An overview,” *Annals of Indian Academy of Neurology*, vol. 15, no. 4, pp. 239–246, 2012, doi: 10.4103/0972-2327.104323.
- [50] J. J. Knierim, “The hippocampus,” *Curr. Biol.*, vol. 25, no. 23, pp. R1116–R1121, 2015,

doi: 10.1016/j.cub.2015.10.049.

- [51] R. N. Dilger and R. W. Johnson, “Behavioral assessment of cognitive function using a translational neonatal piglet model,” *Brain Behav. Immun.*, vol. 24, no. 7, pp. 1156–1165, 2010, doi: 10.1016/j.bbi.2010.05.008.
- [52] S. Shroff, “Putamen,” in *Encyclopedia of Clinical Neuropsychology*, 2011, pp. 2091–2092.
- [53] L. Schmitt, “Caudate Nucleus,” in *Encyclopedia of Autism Spectrum Disorders*, 2013, pp. 538–544.
- [54] S. Shultz, “Putamen,” in *Encyclopedia of Autism Spectrum Disorders*, 2013, pp. 2482–2482.
- [55] W. G. Herrera, M. Bento, and L. Rittner, “Corpus Callosum Shape Signature for Segmentation Evaluation,” in *International Federation for Medical and Biological Engineering Proceeding*, vol. 70, no. 2, Springer Singapore, 2019, pp. 143–147.
- [56] J. Drouin, “Pituitary Development,” in *The Pituitary*, Fourth Edi., Elsevier Inc., 2020, pp. 1–22.
- [57] O. Beck, G. Jonsson, and A. Lundman, “5-Methoxyindoles in Pineal Gland of Cow, Pig, Sheep and Rat,” *Naunyn. Schmiedeberg's Arch. Pharmacol.*, vol. 318, no. 1981, pp. 49–55, 1981.
- [58] J. Song, “Pineal gland dysfunction in Alzheimer ’ s disease : relationship with the immune-pineal axis , sleep disturbance , and neurogenesis,” *Mol. Neurodegener.*, vol. 14, no. 28, pp. 1–10, 2019.
- [59] J. Stiles and T. L. Jernigan, “The Basics of Brain Development,” *Neuropsychol. Rev.*, vol. 20, pp. 327–348, 2010, doi: 10.1007/s11065-010-9148-4.

- [60] M. H. Johnson, “FUNCTIONAL BRAIN DEVELOPMENT IN HUMANS,” *Nat. Rev. Neurosci.*, vol. 2, pp. 475–483, 2001.
- [61] J. Dobbing and J. Sands, “Quantitative growth and development of human brain,” *Arch. Dis. Child.*, vol. 48, no. 10, pp. 757–767, 1973, doi: 10.1136/adc.48.10.757.
- [62] H. T. Epstein, “Stages in human brain development,” *Dev. Brain Res.*, vol. 30, no. 1, pp. 114–119, 1986, doi: 10.1016/0165-3806(86)90139-2.
- [63] D. Holland *et al.*, “Structural growth trajectories and rates of change in the first 3 months of infant brain development,” *JAMA Neurol.*, vol. 71, no. 10, pp. 1266–1274, 2014, doi: 10.1001/jamaneurol.2014.1638.
- [64] D. J. Simmonds, M. N. Hallquist, M. Asato, and B. Luna, “Developmental stages and sex differences of white matter and behavioral development through adolescence: A longitudinal diffusion tensor imaging (DTI) study,” *Neuroimage*, vol. 92, pp. 356–368, 2014, doi: 10.1016/j.neuroimage.2013.12.044.
- [65] J. Jelsing, R. Nielsen, A. K. Olsen, N. Grand, R. Hemmingsen, and B. Pakkenberg, “The postnatal development of neocortical neurons and glial cells in the Göttingen minipig and the domestic pig brain,” *J. Exp. Biol.*, vol. 209, pp. 1454–1462, 2006, doi: 10.1242/jeb.02141.
- [66] N. A. Goriounova *et al.*, “Large and fast human pyramidal neurons associate with intelligence,” *Elife*, vol. 7, no. e41714, pp. 1–21, 2018, doi: 10.7554/eLife.41714.
- [67] W. D. Hopkins, X. Li, and N. Roberts, “More intelligent chimpanzees (Pan troglodytes) have larger brains and increased cortical thickness,” *Intelligence*, vol. 74, no. August 2018,

- pp. 18–24, 2019, doi: 10.1016/j.intell.2018.11.002.
- [68] A. W. Toga and P. M. Thompson, “Genetics of Brain Structure and Intelligence,” *Annu. Rev. Neurosci.*, vol. 28, pp. 1–23, 2005, doi: 10.1146/annurev.neuro.28.061604.135655.
 - [69] J. Dobbing and J. Sands, “Comparative aspects of the brain growth spurt,” *Early Hum. Dev.*, vol. 3, no. 1, pp. 79–83, 1979, doi: 10.1016/0378-3782(79)90022-7.
 - [70] J. W. Dickerson and J. Dobbing, “Prenatal and postnatal growth and development of the central nervous system of the pig,” *Proc. R. Soc. Lond. B. Biol. Sci.*, vol. 166, no. 1005, pp. 384–395, 1967, doi: 10.1098/rspb.1967.0002.
 - [71] E. C. Radlowski *et al.*, “A neonatal piglet model for investigating brain and cognitive development in small for gestational age human infants,” *PLoS One*, vol. 9, no. 3, 2014, doi: 10.1371/journal.pone.0091951.
 - [72] L. Konkel, “The brain before birth: Using fMRI to explore the secrets of fetal neurodevelopment,” *Environ. Health Perspect.*, vol. 126, no. 11, pp. 1–5, 2018, doi: 10.1289/EHP2268.
 - [73] C. Studholme, “Mapping the developing human brain in utero using quantitative MR imaging techniques,” *Semin Perinatol.*, vol. 39, no. 2, pp. 105–112, 2015, doi: 10.1053/j.semperi.2015.01.003.Mapping.
 - [74] C. R. Bjarkam, A. N. Glud, D. Orlowski, J. C. H. Sørensen, and N. Palomero-Gallagher, “The telencephalon of the Göttingen minipig, cytoarchitecture and cortical surface anatomy,” *Brain Struct. Funct.*, vol. 222, no. 5, pp. 2093–2114, 2017, doi: 10.1007/s00429-016-1327-5.

- [75] B. R. Kornum and G. M. Knudsen, “Cognitive testing of pigs (*Sus scrofa*) in translational biobehavioral research,” *Neurosci. Biobehav. Rev.*, vol. 35, no. 3, pp. 437–451, 2011, doi: 10.1016/j.neubiorev.2010.05.004.
- [76] B. Félix *et al.*, “Stereotaxic atlas of the pig brain,” *Brain Res. Bull.*, vol. 49, no. 1–2, pp. 1–137, 1999, doi: 10.1016/S0361-9230(99)00012-X.
- [77] S. P. Yun *et al.*, “Magnetic resonance imaging evaluation of Yukatan minipig brains for neurotherapy applications,” *Lab. Anim. Res.*, vol. 27, no. 4, p. 309, 2011, doi: 10.5625/lar.2011.27.4.309.
- [78] S. Saikali *et al.*, “A three-dimensional digital segmented and deformable brain atlas of the domestic pig,” *J. Neurosci. Methods*, vol. 192, no. 1, pp. 102–109, 2010, doi: 10.1016/j.jneumeth.2010.07.041.
- [79] V. Schmidt, *Comparative anatomy of the pig brain - An integrative magnetic resonance imaging (MRI) study of the porcine brain with special emphasis on the external morphology of the cerebral cortex*. 2015.
- [80] M. S. Conrad, R. N. Dilger, A. Nickolls, and R. W. Johnson, “Magnetic resonance imaging of the neonatal piglet brain,” *Pediatr. Res.*, vol. 71, no. 2, pp. 179–184, 2012, doi: 10.1038/pr.2011.21.
- [81] A. Mackenzie-Graham, “In vivo vs. ex vivo magnetic resonance imaging in mice,” *Front. Neuroinform.*, vol. 6, no. 19, p. 1, 2012, doi: 10.3389/fninf.2012.00019.
- [82] S. Jacobson, Elliott M. Marcus, and S. Pugsley, “Diencephalon,” in *Neuroanatomy for the Neuroscientist*, 7th Editio., 2018, pp. 241–267.

- [83] L. W. Swanson, “Mapping the human and future,” *Trends Neurosci.*, vol. 18, no. 11, pp. 471–474, 1995.
- [84] M. K. Georgieff, “Nutrition and the developing brain: Nutrient priorities and measurement,” *Am. J. Clin. Nutr.*, vol. 85, no. 2, pp. 614–620, 2007, doi: 10.1093/ajcn/85.2.614S.
- [85] S. Herculano-Houzel, P. R. Manger, and J. H. Kaas, “Brain scaling in mammalian evolution as a consequence of concerted and mosaic changes in numbers of neurons and average neuronal cell size,” *Front. Neuroanat.*, vol. 8, no. 77, pp. 1–28, 2014, doi: 10.3389/fnana.2014.00077.
- [86] C. D. J. Romero and V. Borrell, “Coevolution of Radial Glial Cells and the Cerebral Cortex,” *Glia*, vol. 63, no. 8, pp. 1303–1319, 2015, doi: 10.1002/glia.22827.
- [87] L. H. Somerville, “Searching for Signatures of Brain Maturity : What Are We Searching For ?,” *Neuron*, vol. 92, no. 6, pp. 1164–1167, 2016, doi: 10.1016/j.neuron.2016.10.059.
- [88] S. Herculano-Houzel, “Numbers of neurons as biological correlates of cognitive capability,” *Curr. Opin. Behav. Sci.*, vol. 16, pp. 1–7, 2017, doi: 10.1016/j.cobeha.2017.02.004.
- [89] P. L. Ackerman, M. E. Beier, M. O. Boyle, and F.-- Phillip, “Working Memory and Intelligence : The Same or Different Constructs ?,” *Psychol. Bull.*, vol. 131, no. 1, pp. 30–60, 2005, doi: 10.1037/0033-2909.131.1.30.
- [90] H. E. Holmes *et al.*, “Comparison of In Vivo and Ex Vivo MRI for the Detection of Structural Abnormalities in a Mouse Model of Tauopathy,” *Front. Neuroinform.*, vol. 11, no. 20, pp. 1–15, 2017, doi: 10.3389/fninf.2017.00020.
- [91] C. Tempel-Brami, Y. S. Schiffenbauer, A. Nyska, N. Ezov, I. Spector, R. Abramovitch and

- R. R. Maronpot, “Practical Applications of in Vivo and ex Vivo MRI in Toxicologic Pathology Using a Novel High-performance Compact MRI System,” *Toxicol. Pathol.*, vol. 43, no. 5, pp. 633–650, 2015, doi: 10.1177/0192623314568390.
- [92] J. P. Lerch, L. Gazdzinski, J. Germann, J. G. Sled, R. M. Henkelman, and B. J. Nieman, “Wanted dead or alive ? The tradeoff between in-vivo versus ex-vivo MR brain imaging in the mouse,” *Front. Neuroinform.*, vol. 6, no. 6, pp. 1–9, 2012, doi: 10.3389/fninf.2012.00006.
- [93] A. S. Shatil, M. N. Uddin, K. M. Matsuda, and C. R. Figley, “Quantitative Ex Vivo Mri changes due to Progressive Formalin Fixation in Whole human Brain specimens : longitudinal characterization of Diffusion , relaxometry , and Myelin Water Fraction Measurements at 3T,” *Front. Neuroinform.*, vol. 5, no. 31, pp. 1–15, 2018, doi: 10.3389/fmed.2018.00031.
- [94] L. E. M. Wisse *et al.*, “Comparison of In Vivo and Ex Vivo MRI of the Human Hippocampal Formation in the Same Subjects,” *Cereb. Cortex*, vol. 27, no. 11, pp. 5185–5196, 2017, doi: 10.1093/cercor/bhw299.
- [95] D. Giavarina, “Understanding Bland Altman analysis,” *Biochem. Medica*, vol. 25, no. 2, pp. 141–51, 2014, doi: 10.1201/b16720-37.
- [96] N. Ö. Doğan, “Bland-Altman analysis: A paradigm to understand correlation and agreement,” *Turkish J. Emerg. Med.*, vol. 18, no. 4, pp. 139–141, 2018, doi: 10.1016/j.tjem.2018.09.001.

8. VITA

- Name:** Szumo Wang
- Education background:** M.S., Bioengineering
University of Illinois at Chicago, Chicago, IL
B.S., Microbiology, Immunology and Biopharmaceuticals, June 2016
National Chiayi University, Chiayi, Taiwan (ROC)
- Research experiment:**
- The association of insertion sequences with carbapenem resistance and plasmid incompatibility groups in different *Klebsiella pneumoniae* genotypes, 2014 – 2015
 - Ultrahigh-field 9.4T MRI for evaluating neonatal piglet brain, 2019 – 2021
- Work experiment:** Lab Assistant of Microbiological Lab (February – June, 2015)
Lab Assistant of Basic Biotechnology Lab (July, 2015)
- Conference paper:**
- **Wang S.**, Yan S., Liahg Y, Lee C., and Chu C. (August, 2015). “The Insertion Sequences, Plasmid Incompatibility Groups, and Genotypes in Clinical *Klebsiella pneumonia*”. Poster was presented at the 20th Conference of Bacteriology, Tainan, ROC.
 - **Szumo Wang**, Yimin Chen, Jin Gao, Kevin Hu, Riken Patel, Kelly Tappenden, Weiguo Li. (November, 2020) “A Neonatal Piglet Brain Database with High Resolution MRI”.

Poster was presented at ASMRM & ICMRI 2020
Conference, Republic of Korea. (Virtual Conference)

Professional membership: Taiwan Society of Microbiology, ROC (2014 – 2015)
Radiological Society of North America (2018 – 2020)
Asian Society of Magnetic Resonance in Medicine, South Korea
(2020 – 2021)